2011

Modeling, comparison and analysis of multi body parafoil models with varying degrees of freedom

Chrystine M. Gorman

MODELING, COMPARISON AND ANALYSIS OF MULTI-BODY PARAFOIL MODELS WITH VARYING DEGREES OF FREEDOM

by

CHRYSTINE M. GORMAN

A DISSERTATION

Submitted in partial fulfillment of the requirements
for the degree of Doctor of Philosophy
in
The Department of Mechanical and Aerospace Engineering
to
The School of Graduate Studies
of
The University of Alabama in Huntsville

HUNTSVILLE, ALABAMA

2011

In presenting this dissertation in partial fulfillment of the requirements for a doctoral degree from The University of Alabama in Huntsville, I agree that the Library of this University shall make it freely available for inspection. I further agree that permission for extensive copying for scholarly purposes may be granted by my advisor or, in his/her absence, by the Chair of the Department or the Dean of the School of Graduate Studies. It is also understood that due recognition shall be given to me and to The University of Alabama in Huntsville in any scholarly use which may be made of any material in this dissertation.

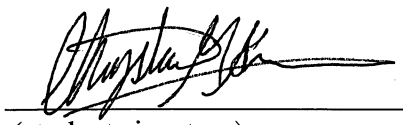

(student signature) 7-12-2011 (date)

DISSERTATION APPROVAL PAGE

Submitted by Chrystine Gorman in partial fulfillment of the requirements for the degree of Doctor of Philosophy in Mechanical Engineering and accepted on behalf of the Faculty of the School of Graduate Studies by the dissertation committee.

We, the undersigned members of the Graduate Faculty of The University of Alabama in Huntsville, certify that we have advised and/or supervised the candidate on the work described in this dissertation. We further certify that we have reviewed the dissertation manuscript and approve it in partial fulfillment of the requirements for the degree of Doctor of Philosophy in Mechanical Engineering.

7-12-2011 Committee Chair
(Date)

7/14/11

7/14/11

7/14/11

7/15/11

7/15/11 Department Chair

07/18/11 College Dean

11/29/11 Graduate Dean

ABSTRACT

The School of Graduate Studies
The University of Alabama in Huntsville

Degree Doctor of Philosophy

College/Dept. Engineering/Mechanical and Aerospace Engineering

Name of Candidate Chrystine M. Gorman

Title Modeling, Comparison and Analysis of Multi-body Parafoil Models with Varying Degrees of Freedom

Guided parafoils are comprised of two primary bodies, a payload and parafoil. While the parafoil generates the majority of aerodynamic loads, the sensor systems used for guidance are located away from the parafoil near the payload. Using Newtonian dynamics, models ranging from six to nine degrees-of-freedom were developed in parallel. For the first time, miniature wireless sensors were developed to investigate the canopy and payload during flight and to directly measure the parafoil-payload relative motion to verify the models. Experimental data was compared to models to investigate and determine system configuration dynamics that could affect the parafoil control system and its corresponding degree-of-freedom model. In addition, classical flight modes similar to those in aircraft flight dynamics were developed for the conventional rigid parafoil-payload system for the first time which include short period and phugoid longitudinal modes and roll subsidence, spiral, and dutch roll lateral modes. Similar linearization of a seven degree-of-freedom model was shown to have an additional lightly damped lateral payload mode.

Abstract Approval: Committee Chair _____

Department Chair _____

Graduate Dean _____

ACKNOWLEDGMENTS

I would like to express my gratitude to my advisor, Dr. Nathan Slegers, for his direction, help, and patience and especially for the gift of knowledge and critical thinking that I will take with me into the future. I would like to thank my committee, Dr. Hugh Coleman, Dr. Farbod Fahimi, Dr. Brian Landrum, Dr. Ken Zuo, for their recommendations and guidance. I would also like convey my appreciation to the MAE Department and its staff for their assistance and support. Finally, I would like to thank my friends for their backing and incredible thesaurus skills and my family for their encouragement and constant support.

Without you, the work developed in this dissertation would not have been possible. Thank you.

TABLE OF CONTENTS

LIST OF FIGURES

List of Tables

LIST OF ABBREVIATIONS/ACRONYMS

AFFDL - Air Force Flight Dynamics Laboratory

DOF - Degree of Freedom

FBD - Free Body Diagram

GNC - Guidance, Navigation and Control

GPS - Global Position System

KD - Kinetic Diagram

NASA - National Aeronautics and Space Administration

LIST OF SYMBOLS

A, B, C, P, Q, R	=	Lamb's coefficients for apparent mass
$\mathbf{a_{B/I}}$, $\mathbf{a_{S/I}}$	=	mass center accelerations of the parafoil and payload
b	=	canopy span
C_{DS}	=	payload drag coefficient
$\bar{c}$	=	canopy main chord
$\mathbf{E_1}, \mathbf{E_2}$	=	matrix made of the first 1 and 2 columns of the identity matrix
$\mathbf{F_A}, \mathbf{M_A}$	=	parafoil aerodynamic force and moment
$\mathbf{F_{AM}}, \mathbf{M_{AM}}$	=	apparent mass force and moment
$\mathbf{F_c}, \mathbf{M_c}$	=	internal constraint force and moment
$\mathbf{F_{W_B}}, \mathbf{F_{W_S}}$	=	parafoil and payload weight
$\mathbf{F_S}$	=	payload drag force
g	=	gravity constant
$\mathbf{H_{B/I}}, \mathbf{H_{S/I}}$	=	parafoil and payload angular momentum
$\mathbf{I_{AM}}$, $\mathbf{I_{AI}}$	=	apparent mass and inertia matrices
$\mathbf{I_B}$, $\mathbf{I_S}$	=	parafoil and payload inertia matrices
$\mathbf{i_B}$, $\mathbf{j_B}$, $\mathbf{k_B}$	=	body frame unit vectors
$\mathbf{i_I}$, $\mathbf{j_I}$, $\mathbf{k_I}$	=	inertial frame unit vectors
$\mathbf{I_{NxN}}$	=	N x N identity matrix
$\mathbf{i_P}$, $\mathbf{j_P}$, $\mathbf{k_P}$	=	canopy frame unit vectors
$\mathbf{i_S}$, $\mathbf{j_S}$, $\mathbf{k_S}$	=	payload frame unit vectors
L_S	=	payload length
M_{cx}, M_{cy}	=	constraint moments in the payload frame

M_{cz}	=	twist constraint moment in the body frame
m_B	=	6-DOF: mass of the parafoil and payload, 7/8/9-DOF: mass of parafoil alone
m_I	=	included mass
m_S	=	mass of the payload
m_{B+I}	=	mass of the parafoil and included mass
$\tilde{p},\ \tilde{q},\ \tilde{r}$	=	aerodynamic angular velocity components in the canopy frame
$p_B,\ q_B,\ r_B$	=	parafoil angular velocity components in the body frame
$p_S,\ q_S,\ r_S$	=	payload angular velocity components in the payload frame
$\mathbf{r_{XY}}$	=	position vector from a point X to a point Y
$\mathbf{S^B_{\omega_B}},\ \mathbf{S^P_{\omega_B}}$	=	cross-product matrices of the parafoil angular velocity in the body and canopy frames.
$\mathbf{S^S_{\omega_S}}$	=	cross-product matrix of the payload expressed in the payload frame
$\mathbf{S^Z_{r_{XY}}}$	=	cross-product matrix of a position vector from a point X to a point Y in the Z frame
$S_A,\ S_S$	=	reference area of the parafoil canopy and payload
$\mathbf{T_{AP}}$	=	transformation from the aerodynamic to the canopy frame
$\mathbf{T_{BP}}$	=	transformation from the body to the canopy frame
$\mathbf{T_{BS}}$	=	transformation from the body to payload frame
$\mathbf{T_{IB}}$	=	transformation from the inertial to body frame
$\tilde{u},\ \tilde{v},\ \tilde{w}$	=	aerodynamic velocity components expressed in the canopy frame
$u_A,\ v_A,\ w_A$	=	canopy aerodynamic velocity components
$u_S,\ v_S,\ w_S$	=	payload aerodynamic velocity components

$u_C,\ v_C,\ w_C$	=	connection point velocity components
$V_A,\ V_S$	=	total aerodynamic speed of the canopy and payload
$\mathbf{V_A^P}$	=	canopy aerodynamic velocity vector expressed in the canopy frame
$\mathbf{V_{A/I}}$	=	wind velocity vector expressed in the inertial frame
$\mathbf{V_S^S}$	=	payload aerodynamic velocity vector expressed in payload frame
$\mathbf{V_C}$	=	velocity vector of connection point *C*
$\mathbf{V_C^B}$	=	velocity vector of connection point *C* expressed in body frame
$x_{XY},\ y_{XY},\ z_{XY}$	=	position vector components from a point X to a point Y
$\alpha,\ \beta$	=	canopy angle of attack and sideslip angle
$\boldsymbol{\alpha}_\mathrm{B}, \boldsymbol{\alpha}_\mathrm{S}$	=	parafoil and payload angular accelerations in their respective frames
Γ	=	canopy incidence angle
δ	=	maximum brake deflection
δ_a	=	asymmetric brake deflection
$\phi_B,\ \theta_B,\ \psi_B$	=	Euler roll, pitch and yaw angles of the parafoil body
$\phi_S,\ \theta_S,\ \psi_S$	=	Euler roll, pitch and yaw angles of the payload
$\boldsymbol{\omega}_\mathrm{B}, \boldsymbol{\omega}_\mathrm{S}$	=	parafoil and payload angular velocities in their respective frames
$\boldsymbol{\omega}_{\mathrm{B/S}}$	=	angular velocity of the payload with respect to the parafoil
$\mathbf{0_{NxN}}$	=	N x N zero matrix

GLOSSARY

Parafoil	fabric airfoil, also used to describe the entire system
Slider	fabric rectangular section used to help control and separate parafoil lines during deployment and inflation
Riser	connection between suspension lines and payload
Suspension Lines	lines connecting canopy to riser
Relative Motion	motion between two objects
Yaw	angular rotation about the z body axis
Pitch	angular rotation about the y body axis
Roll	angular rotation about the x body axis
Decelerator	object that aerodynamically slows decent
Winch	device used to increase or decrease the length of the control lines

CHAPTER 1

INTRODUCTION

Parafoils are similar to airplane wings but are made of light weight flexible material. Parafoil canopies are generally constructed of nylon and have a rectangular planform with an upper and lower surface that forms an airfoil shape. The front of the canopy is open to airflow which moves down fabric channels running between front and back. The airflow exiting is restricted. These channels create cells that inflate when air pressure is greater on the inside than the atmospheric pressure on the outside of the airfoil. Parafoils are a type of decelerator that uses aerodynamic forces to decrease velocity and allow for a softer payload landing. In other words, parafoils use their own weight, aerodynamic forces and geometry to control their decent and trajectory.

As seen in Figure 1.1, parafoils contain several components. The canopy attaches to the suspension lines. The suspension lines are in turn fixed to risers which connect the lines to the payload. A slider generally keeps the suspension lines from getting tangled upon canopy inflation as well as slows the inflation event.

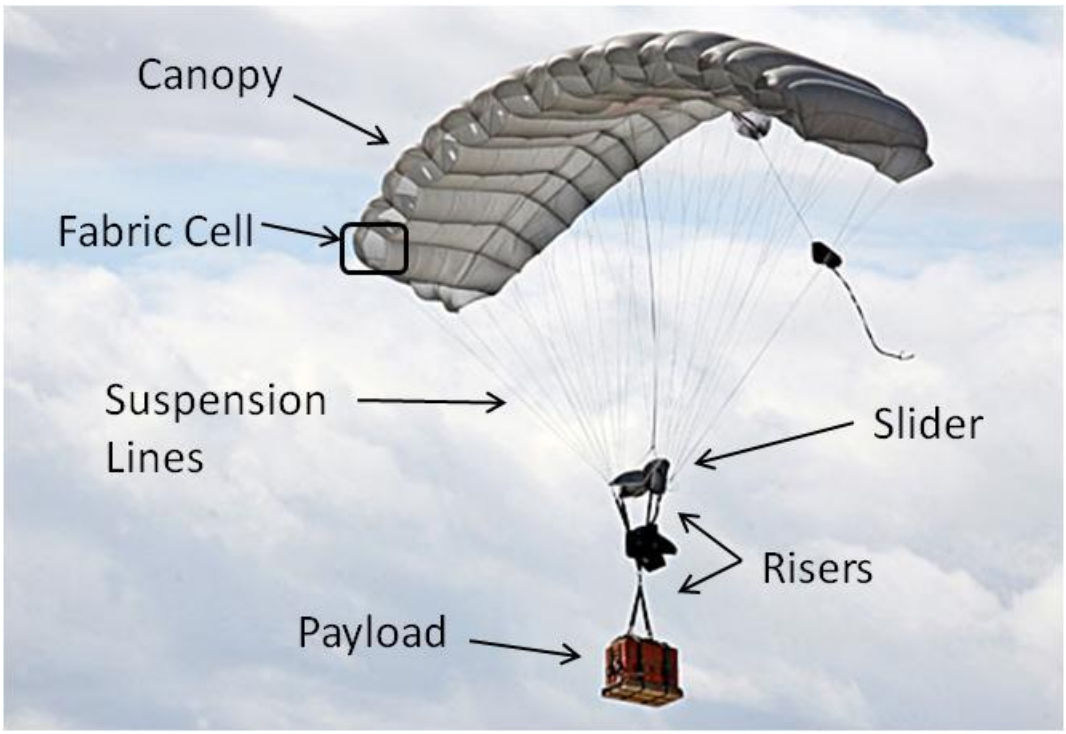

Figure 1.1 Onyx Ultra Light (Onyx UL) [20].

Parafoils can cover large distances both vertically and horizontally to reach their target area at low speeds. Parafoils have been used to perform resupply missions, humanitarian aid, and charting expeditions with reduced danger to the deploying aircraft. They are generally lightweight and display good performance in most standard drop conditions. Other advantages which grant the parafoil widespread usage are its small preflight size and low overhead.

Many aspects of parafoil systems, from the canopy to the payload, make them difficult to accurately model. For instance, the parafoil itself is a flexible fabric airfoil allowing the possibility of changing aerodynamics and canopy shape. In addition, the canopy has a small mass-to-volume ratio resulting in apparent mass forces and moments.

Another significant complication is the payload and canopy interaction. Suspension lines between the parafoil and payload are flexible and can be connected

using many configurations that allow a range of motion from free rotation of the payload with respect to the parafoil to a rigid canopy-payload connection. In some applications, certain characteristics of the parafoil and payload can be ignored resulting in a range of models with varying degrees-of-freedom (DOF). The existence of multi-body parafoil models with varying DOF raises the question, "which one is the most appropriate?"

The simplest model that captures all significant dynamics is desired in engineering applications. In order to provide answers to the above question, the various DOF models must be compared. However, as can be seen in the existing literature, previous models use their own methods and nomenclatures so that each model often has different payload and aerodynamic models, different geometric definitions, and different assumptions and will be difficult to compare. A conventional 6-DOF rigid model is developed in parallel to 7/8/9-DOF models using Newtonian methods and a consistent canopy and payload aerodynamic model along with one set of geometry definitions. Varying DOF models are then developed only by changing the kinematic constraints between the payload and canopy.

A comparison of these models with experimental data determines which models capture the significant dynamics. For autonomous parafoils, control algorithms use parafoil yaw to obtain correct course trajectory and any dynamics which significantly contribute to payload or parafoil yawing can be considered significant. However, measurement of parafoil-payload relative motion is challenging due to the flexible nature of the canopy and requires a sensing system that does not interfere with canopy packing, does not significantly increase the canopy mass, and does not requires physical connection between the canopy and payload.

Miniature low power wireless inertial sensors were developed to be placed in the canopy. After release, the canopy sensors transmit inertial data to a main payload flight computer in flight. Information provided from each sensor includes orientation, angular velocity, and accelerations. The six through nine DOF models are compared with experimental data to show how well each model performs compared to the test system. Furthermore, the 6- and 7-DOF models are investigated in depth using linearization and classical flight dynamics.

CHAPTER 2

BACKGROUND

2.1 Legacy

Leonardo da Vinci is credited with the first recorded design of a decelerator in 1514 [1-2] although he never built his device. His notebook contains a sketch of a parachute with a rigid pyramid frame covered in cloth and can be seen in Figure 2.1. In 1617, Fauste Veranzio jumped from a tower in Venice using a parachute based on da Vinci's design.

Figure 2.1 Drawing from Il Codice Atlantico di Leonardo da Vinci [21].

In the next century, the main use of decelerators was limited to daredevil entertainment such as lowering animals from rooftops [1] and a jump from a balloon in Paris [2]. However, in 1785, the value of a parachute as more than entertainment was demonstrated by Jean Pierre Blachard whose hot air balloon exploded and he used a parachute to escape with his life [1].

Until this time period the parachute design did not differ greatly from da Vinci's design. Blachard worked on a folded silk chute with no rigid frame and in 1797, Andrew

Garnerin is reported to have made the first jump without a rigid frame. Later his parachute made use of a vent, a hole cut in the apex of the canopy, to reduce oscillations. During WWI, the parachute gained a wide spread usage in Europe, Russia and the United States and saved pilot lives [2].

Eventually, the age of modern decelerators begin in the 1930's, when parachutes begin deployment at high altitudes and speeds [1]. In 1963, a kite maker Domina Jalbert, invented the first ram air parafoil [3]. A diagram of that parafoil can be seen in Figure 2.2. The parafoil was described as a "flexible canopy constituting an upper skin" and "including extending ribs" that provide "channels for the flow of air" [4]. The term "parafoil" was coined by researchers at the University of Notre Dame; a combination of the words parachute and airfoil [3].

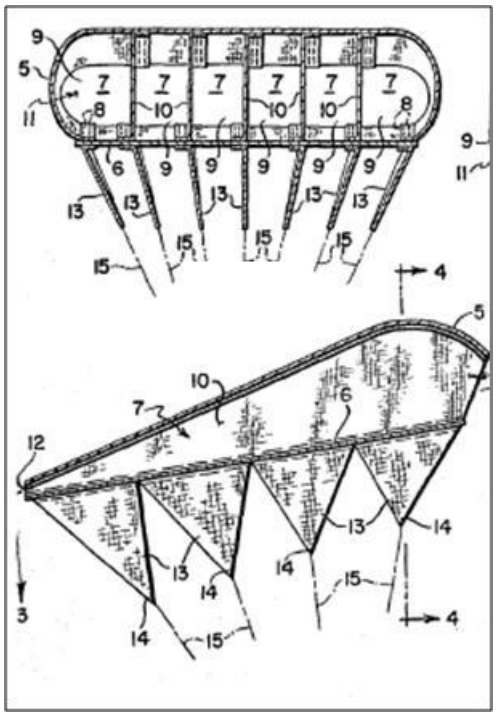

Figure 2.2 Diagrams in Jalbert's patent submitted in 1963 [3].

In 1967, the Air Force Flight Dynamics Laboratory (AFFDL) demonstrated a steerable parafoil/payload system for Project Pin Point [3]. That parafoil carried a 500 lb payload in a controlled flight seen in Figure 2.3.

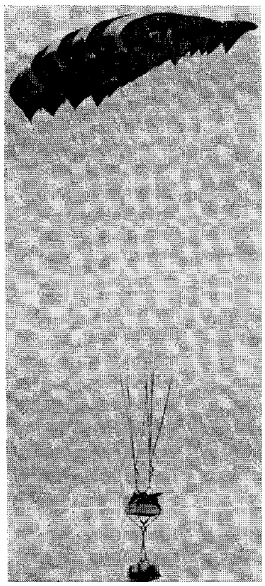

Figure 2.3 Project Pin Point parafoil with 500 lb payload [4].

After the 1970's, parafoils were used for a variety of tasks one of which was payload recovery for sounding rockets. The addition of technology and therefore expense to rockets payloads gave motivation and interest in payload recovery. Other tasks include gathering atmospheric data of Earth's upper atmosphere and military target practice for various weapons [4].

In current parafoil events, the National Aeronautics and Space Administration (NASA) began testing controlled ram-air parafoils for use in spacecraft landing [5] and the United States Military began testing controlled autonomous parafoils for precision troop cargo drops [6]. Parafoils have also begun to have a potential role in the exploration of outer planetary environments, such as the Jupiter atmosphere [7].

2.2 Modeling Literature

Parafoil models have been developed covering a range of DOF approximations. Generally, a low fidelity model such as a kinematic model, reduced order model, or linearized model is used in the design of the Guidance, Navigation and Control (GNC) algorithms. Subsequently, higher fidelity models are employed to evaluate performance in simulation or alternatively in real flight tests.

Simple models include 3-DOF and 4-DOF model developed by Jann [8]. The 3-DOF model is comprised of horizontal ground motion and system heading while the 4-DOF model integrates system roll. The 4-DOF model shows a passable comparison with real flight data.

The next level of complexity is a 6-DOF model where the payload and parafoil are considered one rigid body. A 6-DOF model was developed by Slegers and Costello for use in predictive control [9]. In this model, the parafoil/payload is regarded as a rigid body but the canopy of the parafoil has a small mass-to-volume ratio which results in forces and moments that the model did not include. Barrows developed these apparent mass forces and moments and also accounted for spanwise camber effect [10]. The canopy incidence of a parafoil can also be used for control with Slegers, Beyer, and Costello developing a 6-DOF model that includes changing canopy incidence [11].

Another aspect of parafoil/payload systems is the suspension lines and connection between the canopy and payload. These lines are flexible and can change the geometry and aerodynamics of the parafoil in flight. The variable structure of the parafoil-payload can be simulated by the addition of a confluence plane, axis or point which allows payload and canopy interaction. Figure 2.4 illustrates two different

connections configurations which could be modeled with different DOFs. The possible configurations and their corresponding DOFs will be discussed in greater detail in Chapter 3.

Figure 2.4 Examples of different parafoils, left Guided Parafoil Air Delivery System (GPADS) [21], right is the Joint Precision Air Drop System (JPADS) [22].

Müller, Wagner, and Sachs used an 8-DOF model to evaluate simple maneuvers such as symmetric braking, wind gusts, and payload twist [12]. Redelinghuys developed an 8-DOF model using analytical dynamics which requires artificial constraint stabilization adding differential equations to artificially enforce the constraint forces and moments [13]. Slegers developed an 8-DOF model that allowed the payload to yaw and pitch while solving for constraint forces and moments analytically [14].

Separation of the parafoil and payload by a confluence point instead of a plane allows the payload to freely rotate with respect to the canopy resulting in 9-DOF model. Both Slegers and Costello then Mooij, Wijnands, and Schat developed 9-DOF models for

parafoil systems using different approaches [15-16]. Slegers and Costello used Newtonian dynamics to form the equations of motion resulting in the internal constraint forces at the parafoil and payload connection being automatically solved during simulation. Mooij, Wijnands, and Schat used analytical dynamics requiring artificial constraint stabilization to satisfy the constraint at the point.

Interaction between the parafoil and payload can potentially contribute to system control performance because the system sensors are typically located away from the parafoil canopy. In 2005, Strickert and Jann [16] successfully used video-image processing techniques to measure parafoil-payload relative motion. Post flight analysis demonstrated the difficulty in estimating the differences in the orientation of the payload and canopy.

A noted absence in the literature is that of the 7-DOF model. The following chapter rectifies the lack and develops the 6/8/9-DOF models in parallel to be used for rigorous comparison in the results chapter.

CHAPTER 3

DYNAMIC MODELS

3.1 Model Configuration

Parafoil-payload models can be represented with a variety of different rigging geometries to produce different DOF systems. A 6-DOF model is treated as a rigid body where the connection lines are considered inflexible and solid. The degrees include three inertial position components of the connection point *C* and three Euler orientation angles of the body. As rigging geometry and riser connection change, the connection points to the payload can restrict payload motion. The 7-DOF model payload, Figure 3.1, is connected by four points to the payload at a confluence plane, this connection prohibits roll and pitch relative motion but allows for yawing motion requiring an Euler yaw angle about the z-axis. The 8-DOF two point connection in a confluence axis and permits a yawing and pitching motion but prevents rolling motion and the 9-DOF single point connection and confluence point and allows for all three motions. The degrees of freedom for each model are stated in tabular format in Table 3.1.

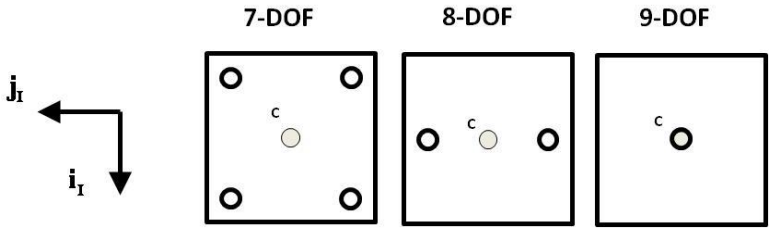

Figure 3.1 Payload top view showing connection points.

Table 3.1. Degrees of Freedom for Each Model

Model	Body	Payload
6-DOF	$x_C, y_C, z_C,$ $\varphi_B, \theta_B, \psi_B$	-
7-DOF	$x_C, y_C, z_C,$ $\varphi_B, \theta_B, \psi_B$	ψ_s
8-DOF	$x_C, y_C, z_C,$ $\varphi_B, \theta_B, \psi_B$	θ_S, ψ_s
9-DOF	$x_C, y_C, z_C,$ $\varphi_B, \theta_B, \psi_B$	$\varphi_S, \theta_S, \psi_s$

If the parafoil-payload system is considered a rigid body as in the 6-DOF model, the parafoil and payload are a single body as seen in Figure 3.2a with only one center of mass. For the 7/8/9-DOF models, Figure 3.2b, the model is considered to have two bodies: the parafoil and the payload with respective centers of mass. The two mass centers located at point B are not in the same location and will be discussed in more detail in the next section.

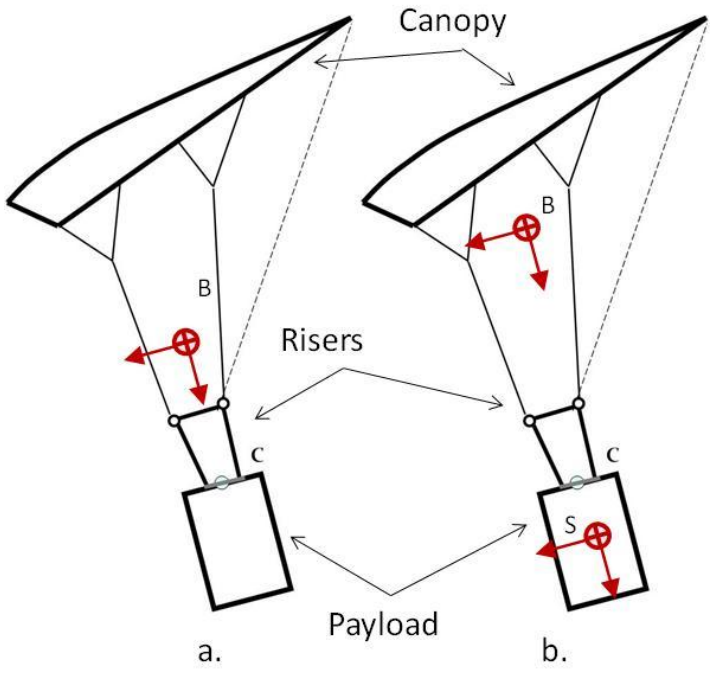

Figure 3.2. Side view showing the difference between the 6-DOF (a) and the 7/8/9-DOF (b).

3.2 Coordinate Frames

Using the 9-DOF two body parafoil-payload system as the base example, shown in Figures 3.3 and 3.4, there are three main coordinate frames required to develop the model. These frames appear in all general parafoil-payload models.

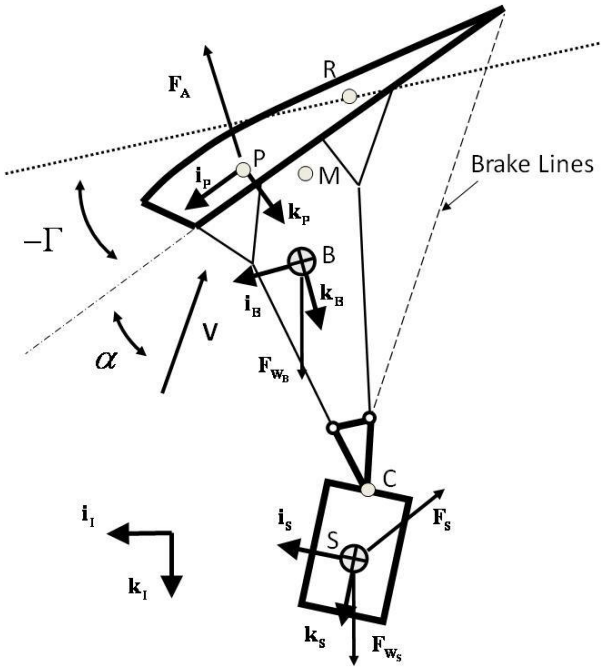

Figure 3.3 Parafoil-payload side view.

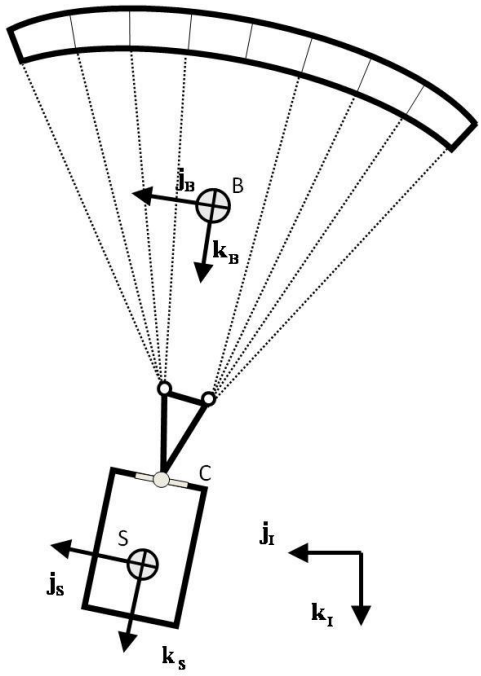

Figure 3.4 Parafoil-payload front view.

For the 6-DOF model, a body frame (B) is fixed at the mass center that includes the canopy, suspension lines, risers and payload. For the 7/8/9-DOF models, the body frame excludes the payload. The body frame orientation is obtained by the conventional aerospace sequence of three body-fixed rotations using Euler yaw ψ_b, pitch θ_b, and roll φ_b starting from the inertial frame. A visual sequence of these rotations can be seen in Figure 3.5.

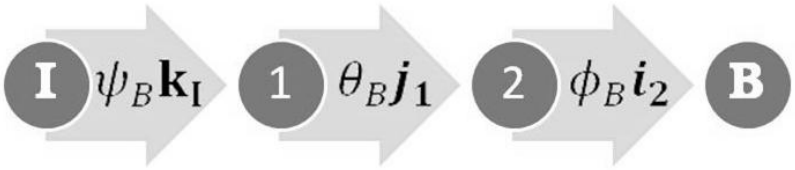

Figure 3.5 Rotations between inertial frame (I) and parafoil body frame (B).

The transformations from the inertial to body frame can be written using common shorthand notation for trigonometric functions of $\sin(\alpha) \equiv s_\alpha$, $\cos(\alpha) \equiv c_\alpha$, and $\tan(\alpha) \equiv t_\alpha$.

$$\mathbf{T_{IB}} = \begin{bmatrix} c_{\theta_B} c_{\psi_B} & c_{\theta_B} s_{\psi_B} & -s_{\theta_B} \\ s_{\phi_B} s_{\theta_B} c_{\psi_B} - c_{\phi_B} s_{\psi_B} & s_{\phi_B} s_{\theta_B} s_{\psi_B} + c_{\phi_B} c_{\psi_B} & s_{\phi_B} c_{\theta_B} \\ c_{\phi_B} s_{\theta_B} c_{\psi_B} + s_{\phi_B} s_{\psi_B} & c_{\phi_B} s_{\theta_B} s_{\psi_B} - s_{\phi_B} c_{\psi_B} & c_{\phi_B} c_{\theta_B} \end{bmatrix} \tag{3.1}$$

A parafoil canopy frame (P) is fixed to the canopy aerodynamic center. Orientation of the parafoil canopy frame with respect to the body frame is defined as the incidence angle Γ about the point R and is a constant for the system which can be seen in Figure 3.3. Similar to the transformation in Equation (3.1) the body frame to parafoil canopy frame can be written as

$$\mathbf{T_{BP}} = \begin{bmatrix} c_\Gamma & 0 & -s_\Gamma \\ 0 & 1 & 0 \\ s_\Gamma & 0 & c_\Gamma \end{bmatrix}. \tag{3.2}$$

The payload frame (S) is fixed at the mass center of the payload and its orientation is dependent on the connection geometry. In the 6-DOF model, orientation angles between the parafoil and payload are considered zero in keeping with the rigid body assumption. However, for the 7-DOF model, payload orientation is obtained by a body-fixed rotation through a Euler yaw angle starting from the body frame.

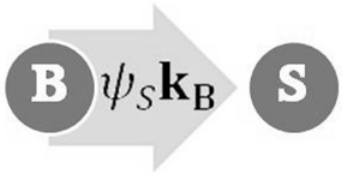

Figure 3.6 Rotations between body frame (B) and payload frame (S) for the 7-DOF system.

The transformation matrix is written as

$$\mathbf{T_{BS}} = \begin{bmatrix} c_{\psi_s} & s_{\psi_s} & 0 \\ -s_{\psi_s} & c_{\psi_s} & 0 \\ 0 & 0 & 1 \end{bmatrix}. \tag{3.3}$$

The 8-DOF payload orientation can be found by two body-fixed rotations, yaw ψ_S, and then pitch θ_S while the 9-DOF is rotated by three relative body-fixed Euler motion angles, ψ_S, θ_S, and ϕ_S.

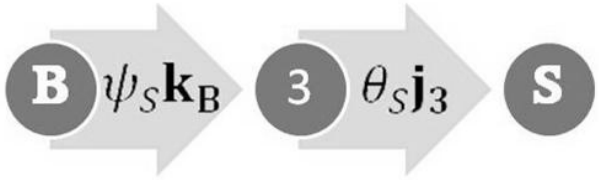

Figure 3.7 Rotations between body frame (B) and payload frame (S) for the 8-DOF system.

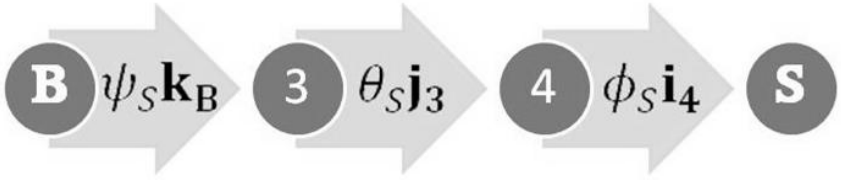

Figure 3.8 Rotations between body frame (B) and payload frame (S) for the 9-DOF system.

These rotations resulting in the following body to payload frame transformations:

$$\mathbf{T_{BS}} = \begin{bmatrix} c_{\theta_s}c_{\psi_s} & c_{\theta_s}s_{\psi_s} & -s_{\theta_s} \\ -s_{\psi_s} & c_{\psi_s} & 0 \\ s_{\theta_s}c_{\psi_s} & s_{\theta_s}s_{\psi_s} & c_{\theta_s} \end{bmatrix} \tag{3.4}$$

$$\mathbf{T_{BS}} = \begin{bmatrix} c_{\theta_S}c_{\psi_S} & c_{\theta_S}s_{\psi_S} & -s_{\theta_S} \\ s_{\phi_S}s_{\theta_S}c_{\psi_S} - c_{\phi_S}s_{\psi_S} & s_{\phi_S}s_{\theta_S}s_{\psi_S} + c_{\phi_S}c_{\psi_S} & s_{\phi_S}c_{\theta_S} \\ c_{\phi_S}s_{\theta_S}c_{\psi_S} + s_{\phi_S}s_{\psi_S} & c_{\phi_S}s_{\theta_S}s_{\psi_S} - s_{\phi_S}c_{\psi_S} & c_{\phi_S}c_{\theta_S} \end{bmatrix}. \tag{3.5}$$

3.3 General Equations of Motion

3.3.1 Kinematics and Dynamics

The velocity vector of the connection point *C* and the angular velocity component of the parafoil body with respect to the inertial frame (I) are defined in the body frame (B)

$$\mathbf{V_c} = u_c\mathbf{i_B} + v_c\mathbf{j_B} + w_c\mathbf{k_B} = \begin{Bmatrix} u_c \\ v_c \\ w_c \end{Bmatrix} \tag{3.6}$$

$$\boldsymbol{\omega_B} = p_B\mathbf{i_B} + q_B\mathbf{j_B} + r_B\mathbf{k_B} = \begin{Bmatrix} p_B \\ q_B \\ r_B \end{Bmatrix}. \tag{3.7}$$

Translation and rotational kinematic equations for the parafoil body can be obtained for each of the 6/7/8/9-DOF systems by using Equation (3.8) and (3.9).

$$\begin{Bmatrix} \dot{x}_c \\ \dot{y}_c \\ \dot{z}_c \end{Bmatrix} = \mathbf{T_{IB}}^T \begin{Bmatrix} u_c \\ v_c \\ w_c \end{Bmatrix} \tag{3.8}$$

$$\begin{Bmatrix} \dot{\phi}_B \\ \dot{\theta}_B \\ \dot{\psi}_B \end{Bmatrix} = \begin{bmatrix} 1 & s_{\theta_B} t_{\theta_B} & c_{\theta_B} t_{\theta_B} \\ 0 & c_{\phi_B} & -s_{\phi_B} \\ 0 & \frac{s_{\phi_B}}{c_{\theta_B}} & \frac{c_{\phi_B}}{c_{\theta_B}} \end{bmatrix} \begin{Bmatrix} p_B \\ q_B \\ r_B \end{Bmatrix}. \tag{3.9}$$

In the 6-DOF model, the parafoil-payload relative motion is zero and Equations (3.7) and (3.9) adequately represents the motion of the payload as well as the parafoil body. Alternatively, when the relative motion is not negligible the payload will have a different angular velocity. An angular velocity of the payload with respect to the inertial frame (I) can be defined in the payload frame (S) and written as

$$\boldsymbol{\omega_S} = p_S \mathbf{i_S} + q_S \mathbf{j_S} + r_S \mathbf{k_S} = \begin{Bmatrix} p_S \\ q_S \\ r_S \end{Bmatrix}. \tag{3.10}$$

The angular velocity for the payload can also be expressed as the combination of angular velocity of the body and the angular velocity of the payload with respect to the body.

$$\boldsymbol{\omega_S} = p_S \mathbf{i_S} + q_S \mathbf{j_S} + r_S \mathbf{k_S} = \mathbf{T_{BS}} \boldsymbol{\omega_B} + \boldsymbol{\omega_{S/B}}. \tag{3.11}$$

The relative angular velocity can then be written as

$$\boldsymbol{\omega_{S/B}} = \boldsymbol{\omega_S} - \mathbf{T_{BS}} \boldsymbol{\omega_B}. \tag{3.12}$$

For each DOF model, the relative angular velocity can be described using Euler angular rates about each rotation axis as seen in Figures 3.6-3.8 and can be written in the payload frame as for the 7/8/9-DOF models respectively.

$$\boldsymbol{\omega_{S/B}} = (\dot{\psi}_S) \mathbf{k_S} \tag{3.13}$$

$$\boldsymbol{\omega}_{\mathbf{S/B}} = \left(-s_{\theta_s}\dot{\psi}_S\right)\mathbf{i_S} + \left(\dot{\theta}_S\right)\mathbf{j_S} + \left(c_{\theta_S}\dot{\psi}_S\right)\mathbf{k_S} \tag{3.14}$$

$$\begin{aligned}\boldsymbol{\omega}_{\mathbf{S/B}} = &\left(\dot{\phi}_S - s_{\theta_s}\dot{\psi}_S\right)\mathbf{i_S} + \left(c_{\theta_s}s_{\phi_s}\dot{\psi}_S + c_{\phi_S}\dot{\theta}_S\right)\mathbf{j_S} \\ &+ \left(c_{\theta_s}c_{\phi_s}\dot{\psi}_S - s_{\phi_S}\dot{\theta}_S\right)\mathbf{k_S}\end{aligned} \tag{3.15}$$

Equating Equation (3.12) to Equations (3.13)-(3.15) respectively, then placing them in matrix format results in

$$\begin{Bmatrix} p_S \\ q_S \\ r_S \end{Bmatrix} - \mathbf{T_{BS}} \begin{Bmatrix} p_B \\ q_B \\ r_B \end{Bmatrix} = \begin{Bmatrix} 0 \\ 0 \\ \dot{\psi}_S \end{Bmatrix} \tag{3.16}$$

$$\begin{Bmatrix} p_S \\ q_S \\ r_S \end{Bmatrix} - \mathbf{T_{BS}} \begin{Bmatrix} p_B \\ q_B \\ r_B \end{Bmatrix} = \begin{Bmatrix} -s_{\theta_s}\dot{\psi}_S \\ \dot{\theta}_S \\ c_{\theta_S}\dot{\psi}_S \end{Bmatrix} \tag{3.17}$$

$$\begin{Bmatrix} p_S \\ q_S \\ r_S \end{Bmatrix} - \mathbf{T_{BS}} \begin{Bmatrix} p_B \\ q_B \\ r_B \end{Bmatrix} = \begin{Bmatrix} \dot{\phi}_S - s_{\theta_s}\dot{\psi}_S \\ c_{\theta_s}s_{\phi_s}\dot{\psi}_S + c_{\phi_S}\dot{\theta}_S \\ c_{\theta_s}c_{\phi_s}\dot{\psi}_S - s_{\phi_S}\dot{\theta}_S \end{Bmatrix}. \tag{3.18}$$

From Equation (3.16) and (3.17), expressions for two constraints on the payload roll and pitch rate and one payload rotation kinematic equation for the 7-DOF system and a single constraint on payload roll rate and two payload kinematic equations for the 8-DOF system can be found. The 7/8-DOF kinematics and constraints can be written in matrix form as

$$\begin{Bmatrix} p_s \\ q_s \\ \dot{\psi}_s \end{Bmatrix} = \begin{bmatrix} -1 & 0 & 0 \\ 0 & -1 & 0 \\ 0 & 0 & 1 \end{bmatrix} \left(\begin{Bmatrix} 0 \\ 0 \\ r_s \end{Bmatrix} - \mathbf{T_{BS}} \begin{Bmatrix} p_B \\ q_B \\ r_B \end{Bmatrix} \right) \tag{3.19}$$

$$\begin{Bmatrix} p_S \\ \dot{\theta}_S \\ \dot{\psi}_S \end{Bmatrix} = \begin{bmatrix} -1 & 0 & -t_{\theta_S} \\ 0 & 1 & 0 \\ 0 & 0 & 1/c_{\theta_S} \end{bmatrix} \left(\begin{Bmatrix} 0 \\ q_S \\ r_S \end{Bmatrix} - \mathbf{T_{BS}} \begin{Bmatrix} p_B \\ q_B \\ r_B \end{Bmatrix} \right). \tag{3.20}$$

In the 9-DOF system, the payload is not constrained and can rotate freely with respect to the body. Therefore, rotation kinematics equations from Equation (3.18) are

$$\begin{Bmatrix} \dot{\phi}_S \\ \dot{\theta}_S \\ \dot{\psi}_S \end{Bmatrix} = \begin{bmatrix} 1 & s_{\theta_S} t_{\theta_S} & c_{\theta_S} t_{\theta_S} \\ 0 & c_{\phi_S} & -s_{\phi_S} \\ 0 & \frac{s_{\phi_S}}{c_{\theta_S}} & \frac{c_{\phi_S}}{c_{\theta_S}} \end{bmatrix} \left(\begin{Bmatrix} p_S \\ q_S \\ r_S \end{Bmatrix} - \mathbf{T_{BS}} \begin{Bmatrix} p_B \\ q_B \\ r_B \end{Bmatrix} \right). \tag{3.21}$$

Translation and rotation dynamic equations of motion are formed by equating the time derivative of linear momentum with total forces and equating the time derivative of angular momentum with the total moment. In other words, the 6-DOF Free Body Diagram (FBD) related to the 6-DOF Kinetic Diagram (KD) results in two equations

$$\mathbf{F_A} + \mathbf{F_{AM}} + \mathbf{F_{W_B}} + \mathbf{F_S} = (m_I + m_B)\mathbf{a_{B/I}} \tag{3.22}$$

$$\begin{aligned} &\mathbf{M_A} + \mathbf{S^B_{r_{CA}} F_A} + \mathbf{M_{AM}} + \mathbf{S^B_{r_{CM}} F_{AM}} + \mathbf{S^B_{r_{CS}} F_S} + \mathbf{S^B_{r_{CB}} F_{W_B}} \\ &= \frac{\mathrm{d}}{\mathrm{dt}} \mathbf{H^B_{B/I}} + (m_I + m_B)\mathbf{S^B_{r_{CB}} a_{B/I}}. \end{aligned} \tag{3.23}$$

It should also be noted that the body weight acts on the body center of mass and includes both the parafoil weight and the payload weight. The convention for the vector cross product of two vectors $\mathbf{r} = [r_x \quad r_y \quad r_z]^T$ and $\mathbf{F} = [F_x \quad F_y \quad F_z]^T$ both expressed in an A

reference frame is written as

$$\mathbf{S}_{\mathbf{r}}^{\mathbf{A}}\mathbf{F} = \begin{bmatrix} 0 & -r_z & r_y \\ r_z & 0 & -r_x \\ -r_y & r_x & 0 \end{bmatrix}. \tag{3.24}$$

Equations of motion for the 7/8/9-DOF model are formed by separating the parafoil body and payload at the confluence exposing the constraint forces $\mathbf{F_C}$ and moments $\mathbf{M_C}$. Four vector equations can be formed, two by equating the time derivative of linear momentum with total forces on each body, and two by equating the time derivative of angular momentum with the total moment on each body about point their respective mass centers.

$$\mathbf{F_A} + \mathbf{F_{AM}} + \mathbf{F_{W_B}} + \mathbf{F_C} = m_B \mathbf{a_{B/I}} \tag{3.25}$$

$$\mathbf{M_A} + \mathbf{S}_{\mathbf{r_{BP}}}^{\mathbf{B}}\mathbf{F_A} + \mathbf{M_{AM}} + \mathbf{S}_{\mathbf{r_{BM}}}^{\mathbf{B}}\mathbf{F_{AM}} + \mathbf{M_C} + \mathbf{S}_{\mathbf{r_{CB}}}^{\mathbf{B}}\mathbf{F_C} = \frac{\mathrm{d}}{\mathrm{dt}}\mathbf{H}_{\mathbf{B/I}}^{\mathbf{B}} \tag{3.26}$$

$$\mathbf{F_{W_S}} + \mathbf{F_S} + \mathbf{F_C} = m_S \mathbf{a_{S/I}} \tag{3.27}$$

$$\mathbf{M_C} + \mathbf{S}_{\mathbf{r_{CS}}}^{\mathbf{S}}\mathbf{F_C} = \frac{\mathrm{d}}{\mathrm{dt}}\mathbf{H}_{\mathbf{B/I}}^{\mathbf{B}}. \tag{3.28}$$

The required accelerations of the body frame (B) and payload frame (S) for all models are

$$\mathbf{a_{B/I}} = \dot{\mathbf{V}}_\mathbf{c} + \mathbf{S}_{\boldsymbol{\omega}_\mathbf{B}}^{\mathbf{B}}\mathbf{V_c} - \mathbf{S}_{\mathbf{r_{CB}}}^{\mathbf{B}}\boldsymbol{\alpha_B} + \mathbf{S}_{\boldsymbol{\omega}_\mathbf{B}}^{\mathbf{B}}\mathbf{S}_{\boldsymbol{\omega}_\mathbf{B}}^{\mathbf{B}}\mathbf{r_{CB}} \tag{3.29}$$

$$\mathbf{a_{S/I}} = \mathbf{T_{BS}}\left(\dot{\mathbf{V}}_\mathbf{c} + \mathbf{S}_{\boldsymbol{\omega}_\mathbf{B}}^{\mathbf{B}}\mathbf{V_c}\right) - \mathbf{S}_{\mathbf{r_{CS}}}^{\mathbf{S}}\boldsymbol{\alpha_S} + \mathbf{S}_{\boldsymbol{\omega}_\mathbf{S}}^{\mathbf{S}}\mathbf{S}_{\boldsymbol{\omega}_\mathbf{S}}^{\mathbf{S}}\mathbf{r_{CS}}. \tag{3.30}$$

The derivative of angular momentum for the parafoil body and payload in their respective frames are expressed as

$$\frac{\mathrm{d}}{\mathrm{dt}}\mathbf{H_{B/I}} = \mathbf{I_B}\dot{\boldsymbol{\omega}}_\mathbf{B} + \mathbf{S}^{\mathbf{B}}_{\boldsymbol{\omega}_\mathbf{B}}\mathbf{I_B}\boldsymbol{\omega}_\mathbf{B} \tag{3.31}$$

$$\frac{\mathrm{d}}{\mathrm{dt}}\mathbf{H_{S/I}} = \mathbf{I_S}\dot{\boldsymbol{\omega}}_\mathbf{S} + \mathbf{S}^{\mathbf{S}}_{\boldsymbol{\omega}_\mathbf{S}}\mathbf{I_S}\boldsymbol{\omega}_\mathbf{S}. \tag{3.32}$$

In the previous equations, known derivatives of kinematic constraints p_S and q_S for the 7-DOF and p_S for the 8-DOF models appear. These derivatives can be found by differentiating the kinematic constraints in Equations (3.19) and (3.20). Each derivative can be written in compact as seen below where Equation (3.33) is for the 7-DOF and Equation (3.34) for the 8-DOF.

$$\begin{Bmatrix}\dot{p}_S\\ \dot{q}_S\\ \dot{r}_S\end{Bmatrix} = \mathbf{G} + \mathbf{K_1}\dot{r}_S + \mathbf{K_2}\begin{Bmatrix}\dot{p}_B\\ \dot{q}_B\\ \dot{r}_B\end{Bmatrix} \tag{3.33}$$

$$\mathbf{G} = \begin{Bmatrix}g_1\\ 0\\ 0\end{Bmatrix}, \mathbf{K_1} = \begin{Bmatrix}0\\ 0\\ 1\end{Bmatrix}, \mathbf{K_2} = \begin{bmatrix}c_{\psi_S} & s_{\psi_S} & 0\\ -s_{\psi_S} & c_{\psi_S} & 0\\ 0 & 0 & 0\end{bmatrix}$$

$$\begin{aligned} g_1 = \left(\frac{1}{c_{\theta_S}^2}\right)\Big[& s_{\theta_S}\left(c_{\psi_S}p_B + S_{\psi_S}q_B\right)q_S + 2\left(c_{\psi_S}q_B - S_{\psi_S}p_B\right)r_S \\ & - q_S r_S + c_{\theta_S}\left(s_{\psi_S}p_B - c_{\psi_S}q_B\right)r_B \\ & + 2s_{\theta_S}s_{\psi_S}c_{\psi_S}(p_B^2 - q_B^2) + 2p_B q_B s_{\theta_S}\left(s_{\psi_S}^2 - c_{\psi_S}^2\right)\Big] \end{aligned}$$

$$\begin{Bmatrix}\dot{p}_S\\ \dot{q}_S\\ \dot{r}_S\end{Bmatrix} = \mathbf{G} + \mathbf{K_1}\begin{Bmatrix}\dot{q}_S\\ \dot{r}_S\end{Bmatrix} + \mathbf{K_2}\begin{Bmatrix}\dot{p}_B\\ \dot{q}_B\\ \dot{r}_B\end{Bmatrix} \tag{3.34}$$

$$\mathbf{G} = \begin{Bmatrix}-s_{\psi_s}(r_S - r_B)p_B + c_{\psi_s}(r_S - r_B)q_B\\ -c_{\psi_s}(r_S - r_B)p_B - s_{\psi_s}(r_S - r_B)q_B\\ 0\end{Bmatrix},$$

$$\mathbf{K_1} = \begin{bmatrix}0 & -t_{\theta_S}\\ 1 & 0\\ 0 & 1\end{bmatrix}, \mathbf{K_2} = \begin{bmatrix}\frac{c_{\psi_S}}{c_{\theta_S}} & \frac{s_{\psi_S}}{c_{\theta_S}} & 0\\ 0 & 0 & 0\\ 0 & 0 & 0\end{bmatrix}.$$

The mass center acceleration of the payload and the time derivative of angular momentum combined with the kinematic constraints in (3.33) and (3.34) become

$$\begin{aligned}\mathbf{a_{S/I}} = \mathbf{T_{BS}}\left(\dot{\mathbf{V}}_\mathbf{c} + \mathbf{S}^{\mathbf{B}}_{\boldsymbol{\omega}_\mathbf{B}}\mathbf{V_c}\right) - \mathbf{S}^{\mathbf{S}}_{\mathbf{r}_{\mathbf{CS}}}\left(\mathbf{G} + \mathbf{K_1}\dot{r}_S + \mathbf{K_2}\begin{Bmatrix}\dot{p}_B\\ \dot{q}_B\\ \dot{r}_B\end{Bmatrix}\right)\\ + \mathbf{S}^{\mathbf{S}}_{\boldsymbol{\omega}_\mathbf{S}}\mathbf{S}^{\mathbf{S}}_{\boldsymbol{\omega}_\mathbf{S}}\mathbf{r_{CS}}\end{aligned} \tag{3.35}$$

$$\frac{\mathrm{d}}{\mathrm{dt}}\mathbf{H_{S/I}} = \mathbf{I_S}\left(\mathbf{G} + \mathbf{K_1}\dot{r}_S + \mathbf{K_2}\begin{Bmatrix}\dot{p}_B\\ \dot{q}_B\\ \dot{r}_B\end{Bmatrix}\right) + \mathbf{S}^{\mathbf{S}}_{\boldsymbol{\omega}_\mathbf{S}}\mathbf{I_S}\boldsymbol{\omega}_\mathbf{S} \tag{3.36}$$

for the 7-DOF model and

$$\begin{aligned}\mathbf{a_{S/I}} = \mathbf{T_{BS}}\left(\dot{\mathbf{V}}_\mathbf{c} + \mathbf{S}^{\mathbf{B}}_{\boldsymbol{\omega}_\mathbf{B}}\mathbf{V_c}\right) - \mathbf{S}^{\mathbf{S}}_{\mathbf{r}_{\mathbf{cS}}}\left(\mathbf{G} + \mathbf{K_1}\begin{Bmatrix}\dot{q}_S\\ \dot{r}_S\end{Bmatrix} + \mathbf{K_2}\begin{Bmatrix}\dot{p}_B\\ \dot{q}_B\\ \dot{r}_B\end{Bmatrix}\right)\\ + \mathbf{S}^{\mathbf{S}}_{\boldsymbol{\omega}_\mathbf{S}}\mathbf{S}^{\mathbf{S}}_{\boldsymbol{\omega}_\mathbf{S}}\mathbf{r_{cS}}\end{aligned} \tag{3.37}$$

$$\frac{\mathrm{d}}{\mathrm{dt}}\mathbf{H_{S/I}} = \mathbf{I_S}\left(\mathbf{G} + \mathbf{K_1}\begin{Bmatrix}\dot{q}_S\\ \dot{r}_S\end{Bmatrix} + \mathbf{K_2}\begin{Bmatrix}\dot{p}_B\\ \dot{q}_B\\ \dot{r}_B\end{Bmatrix}\right) + \mathbf{S^S_{\omega_S}}\mathbf{I_S}\boldsymbol{\omega_S} \tag{3.38}$$

for the 8-DOF model.

3.3.2 Forces and Moments

3.3.2.1 Aerodynamic Forces and Moments

The aerodynamic forces and moments do not change between the 6- to 9-DOF configurations. Velocities of the parafoil aerodynamic center and connection point are expressed in the canopy and body frames while the payload velocity is expressed in the payload frame.

$$\begin{aligned}\mathbf{V_A^P} &= u_A\mathbf{i_P} + v_A\mathbf{j_P} + w_A\mathbf{k_P}\\ \mathbf{V_S^S} &= u_S\mathbf{i_S} + v_S\mathbf{j_S} + w_S\mathbf{k_S}\\ \mathbf{V_C^B} &= u_c\mathbf{i_B} + v_c\mathbf{j_B} + w_c\mathbf{k_B}.\end{aligned} \tag{3.39}$$

The aerodynamic velocity of the parafoil can be found by expressing the parafoil velocity in the canopy frame and subtracting inertial winds. In more detail, the equation becomes

$$\widetilde{\mathbf{V}} = \mathbf{T_{BP}}\left(\mathbf{V_C} + \mathbf{S^B_{\omega_B}}\left(\mathbf{r_{CR}} + \mathbf{T_{BP}}^T\mathbf{r_{RP}}\right) - \mathbf{T_{IB}}\mathbf{V_{A/I}}\right) \tag{3.40}$$

with the aerodynamic angles being defined as

$$\alpha = \mathrm{atan}\left(\frac{\widetilde{w}}{\widetilde{u}}\right) \tag{3.41}$$

$$\beta = \text{asin}\left(\frac{\tilde{v}}{V_A}\right), \tag{3.42}$$

where α is the angle of attack that can be seen in Figure 3.3 and β is the side slip angle that can be seen in Figure 3.9.

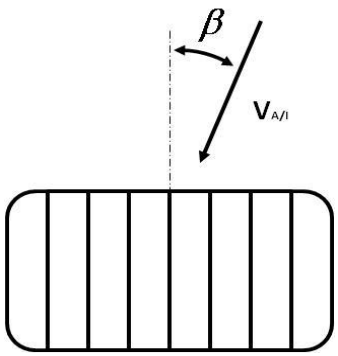

Figure 3.9 Side slip angle definition.

The aerodynamic forces of the parafoil expressed in the body frame can be written as

$$\mathbf{F_A} = \frac{1}{2}\rho V_A^2 S_A \mathbf{T_{BP}}^T \mathbf{T_{AP}} \begin{Bmatrix} C_{D0} + C_{D\alpha^2}\alpha^2 \\ C_{Y\beta}\beta \\ C_{L0} + C_{L\alpha}\alpha \end{Bmatrix}, \tag{3.43}$$

where $\mathbf{T_{AP}}$ is the transformation of the aerodynamic frame to the parafoil frame by the angle α [11, 18]. Similarly for the payload drag,

$$\mathbf{F_S} = -\frac{1}{2}\rho V_S S_S \mathbf{T_{BS}}^T C_{Ds} \begin{Bmatrix} u_S \\ v_S \\ w_S \end{Bmatrix}. \tag{3.44}$$

Aerodynamic moments on the parafoil and payload can be expressed in their respective and are given in (3.45) and (3.46).

$$\mathbf{M_A} = \frac{1}{2}\rho V_A^2 S_A \mathbf{T_{BP}}^T \begin{Bmatrix} b\left(C_{lp}\tilde{p}\left(\frac{b}{2V_A}\right) + C_{l\delta a}\left(\frac{\delta_a}{\delta}\right)\right) \\ \bar{c}\left(C_{m0} + C_{mq}\tilde{q}\left(\frac{\bar{c}}{2V_A}\right)\right) \\ b\left(C_{nr}\tilde{r}\left(\frac{b}{2V_A}\right) + C_{n\delta a}\left(\frac{\delta_a}{\delta}\right)\right) \end{Bmatrix}. \quad (3.45)$$

3.3.2.2 Apparent Mass Forces and Moments

Apparent mass forces and moments are generally negligible for most bodies. However, for parafoils, where the internal air mass is equivalent to the mass of the parafoil, forces and moments generated from accelerating the parafoil through air are significant. Similar to the aerodynamic translational velocity, the angular velocity of the parafoil is expressed in the parafoil frame

$$\begin{Bmatrix} \tilde{p} \\ \tilde{q} \\ \tilde{r} \end{Bmatrix} = \mathbf{T_{BP}} \begin{Bmatrix} p_B \\ q_B \\ r_B \end{Bmatrix}. \quad (3.46)$$

Forces and moments from apparent mass and inertia are found by relating the fluids kinetic energy to the resultant forces and moments [1]. The apparent mass terms are expressed in the body frame and can be written as

$$\mathbf{F_{AM}} = -\mathbf{T_{BP}}^T \left(\mathbf{I_{AM}} \begin{Bmatrix} \dot{\tilde{u}} \\ \dot{\tilde{v}} \\ \dot{\tilde{w}} \end{Bmatrix} + \mathbf{S^P_{\omega_B}} \mathbf{I_{AM}} \begin{Bmatrix} \tilde{u} \\ \tilde{v} \\ \tilde{w} \end{Bmatrix} \right) \quad (3.47)$$

$$\mathbf{M_{AM}} = -\mathbf{T_{BP}}^T \left(\mathbf{I_{AI}} \begin{Bmatrix} \dot{\tilde{p}} \\ \dot{\tilde{q}} \\ \dot{\tilde{r}} \end{Bmatrix} + \mathbf{S^P_{\omega_B}} \mathbf{I_{AI}} \begin{Bmatrix} \tilde{p} \\ \tilde{q} \\ \tilde{r} \end{Bmatrix} \right), \quad (3.48)$$

where the apparent mass and inertia matrix are

$$\mathbf{I_{AM}} = \begin{bmatrix} A & 0 & 0 \\ 0 & B & 0 \\ 0 & 0 & C \end{bmatrix} \tag{3.49}$$

$$\mathbf{I_{AI}} = \begin{bmatrix} P & 0 & 0 \\ 0 & Q & 0 \\ 0 & 0 & R \end{bmatrix}. \tag{3.50}$$

The constants *A, B, C, P, Q,* and *R* can be calculated for simple shapes or approximated [1]. For the assumed configuration, the apparent mass forces and moments act at the apparent mass center and do not change with rigging configuration.

3.3.2.3 Weight Forces and Moments

The weight of the body is written in the body frame (B). The weight forces are of each DOF is dependent on the definition of mass, m_B, which in Equation (3.51) includes the canopy, lines, rigging and payload for the 6-DOF combine model and excludes the payload for the 7/8/9-DOF.

$$\mathbf{F_{W_B}} = m_B g \begin{Bmatrix} -S_{\theta_B} \\ S_{\phi_B} C_{\theta_B} \\ C_{\phi_B} C_{\theta_B} \end{Bmatrix}. \tag{3.51}$$

The 7/8/9-DOF model includes the weight of the payload expressed in the payload frame (S) given as

$$\mathbf{F_{W_S}} = m_S g \mathbf{T_{BS}} \begin{Bmatrix} -S_{\theta_B} \\ S_{\phi_B} C_{\theta_B} \\ C_{\phi_B} C_{\theta_B} \end{Bmatrix}. \tag{3.52}$$

3.3.2.4 Constraint Forces and Moments

The internal constraint forces and moments expressed in the body frame are different for each model based on geometry of the connection lines and are defined as

$$\mathbf{F_c} = F_{cx}\mathbf{i_B} + F_{cy}\mathbf{j_B} + F_{cz}\mathbf{k_B} = \begin{Bmatrix} F_{cx} \\ F_{cy} \\ F_{cz} \end{Bmatrix} \tag{3.53}$$

$$\mathbf{M_c} = \mathbf{T_{BS}}^T \begin{Bmatrix} M_{cx} \\ M_{cy} \\ 0 \end{Bmatrix} + \begin{Bmatrix} 0 \\ 0 \\ M_{cz} \end{Bmatrix} \tag{3.54}$$

$$\mathbf{M_c} = \mathbf{T_{BS}}^T \begin{Bmatrix} M_{cx} \\ 0 \\ 0 \end{Bmatrix} + \begin{Bmatrix} 0 \\ 0 \\ M_{cz} \end{Bmatrix}, \tag{3.55}$$

where Equation (3.54) defines $\mathbf{M_C}$ for the 7-DOF system and Equation (3.55) defines $\mathbf{M_C}$ for the 8-DOF system. The 7/8-DOF models have two and one unknown constraint components, respectively, which may be solved with the dynamic equations. The components of $\mathbf{M_C}$ can be separated into components which must be solved, M_{cx} and M_{cy}, and known moments, M_{cz} as

$$\mathbf{M_c} = \begin{Bmatrix} 0 \\ 0 \\ M_{cz} \end{Bmatrix} + \mathbf{T_{BS}}^T \begin{bmatrix} 1 & 0 \\ 0 & 1 \\ 0 & 0 \end{bmatrix} \begin{Bmatrix} M_{cx} \\ M_{cy} \end{Bmatrix} = \begin{Bmatrix} 0 \\ 0 \\ M_{cz} \end{Bmatrix} + \mathbf{T_{BS}}^T \mathbf{E_2} \begin{Bmatrix} M_{cx} \\ M_{cy} \end{Bmatrix} \tag{3.56}$$

$$\mathbf{M_c} = \begin{Bmatrix} 0 \\ 0 \\ M_{cz} \end{Bmatrix} + \mathbf{T_{BS}}^T \begin{bmatrix} 1 \\ 0 \\ 0 \end{bmatrix} \{M_{cx}\} = \begin{Bmatrix} 0 \\ 0 \\ M_{cz} \end{Bmatrix} + \mathbf{T_{BS}}^T \mathbf{E_1} \{M_{cx}\}. \tag{3.57}$$

where M_{cz} is the known line twist moment and is dependent on the parafoil-payload connection and riser geometry and can vary dramatically from system to system. In this

case, the line twist is modeled as a nonlinear rotational spring and damper where both the stiffness K_ψ and damping coefficients K_r may be functions of ψ_s

$$M_{cz} = K_\psi(\psi_s)\psi_s + K_r(\psi_S)r_s. \tag{3.58}$$

3.3.3 Final Equations of Motion

The dynamic equations of motion, constraint forces, and moments may be found using Newtonian dynamics in the Force/Acceleration Method as previously discussed and can be written as a condensed matrix of the form

$$\mathbf{L}\dot{\mathbf{x}} = \mathbf{B}, \tag{3.59}$$

where each row equation is found by either equating the sum of forces to the derivative of linear momentum or equating a moment summation forces to the derivative of angular momentum. The 6-DOF dynamic equations of motion can be written in matrix form as six equations which can be partitioned into a block 2 x 2 L matrix and a block 2 x 1 B matrix. The first row equation can be found by summing the forces on the parafoil body and second equation is obtained by summing the moments about the connection point *C*.

$$\begin{bmatrix} -\mathbf{I'_{AM}}\mathbf{S^B_{r_{cM}}} - m_{B+I}\mathbf{S^B_{r_{cB}}} & m_{B+I}\mathbf{I_{3x3}} + \mathbf{I'_{AM}} \\ \mathbf{I_B} + \mathbf{I'_{AI}} - \mathbf{S^B_{r_{CM}}}\mathbf{I'_{AM}}\mathbf{S^B_{r_{CM}}} - m_{B+I}\mathbf{S^B_{r_{CB}}}\mathbf{S^B_{r_{CB}}} & m_{B+I}\mathbf{S^B_{r_{CB}}} - \mathbf{S^B_{r_{CM}}}\mathbf{I'_{AM}} \end{bmatrix} \begin{Bmatrix} \dot{p}_B \\ \dot{q}_B \\ \dot{r}_B \\ \cdots \\ \dot{u}_c \\ \dot{v}_c \\ \dot{w}_c \end{Bmatrix} = \begin{Bmatrix} \mathbf{B_1} \\ \cdots \\ \mathbf{B_2} \end{Bmatrix}, \tag{3.60}$$

where

$$\mathbf{B_1} = \mathbf{F_A} + \mathbf{F_S} + \mathbf{F_{W_B}} + m_{B+I}\mathbf{S^B_{\omega_B}V_c} - m_{B+I}\mathbf{S^B_{\omega_B}S^B_{\omega_B}r_{cB}} - m_{B+I}\mathbf{T_{BP}}^{\boldsymbol{T}}\mathbf{S^P_{\omega_B}I_{AM}}\widetilde{\mathbf{V}} - \mathbf{I'_{AM}S^B_{\omega_B}T_{IB}V_{A/I}} \tag{3.61}$$

$$\mathbf{B_2} = \mathbf{M_A} + \mathbf{S^B_{r_{cA}}F_A} + \mathbf{S^B_{r_{CS}}F_S} + \mathbf{S^B_{r_{CB}}F_{W_B}} - \mathbf{S^B_{r_{CM}}T_{BP}}^{\boldsymbol{T}}\mathbf{S^P_{\omega_B}I_{AM}}\widetilde{\mathbf{V}} - \mathbf{T_{BP}}^{\boldsymbol{T}}\mathbf{S^P_{\omega_B}I_{AI}}\widetilde{\boldsymbol{\omega}} - \mathbf{S^B_{r_{cM}}I'_{AM}S^B_{\omega_B}T_{IB}V_{A/I}} - \mathbf{S^B_{\omega_B}I_B\omega_B}. \tag{3.62}$$

The common convection of $\mathbf{I'_x} = \mathbf{T_{BP}}^{\boldsymbol{T}}\mathbf{I_xT_{BP}}$ is used for simplicity. Also, the shorthand notation for $(m_I + m_B)$ is m_{B+I} and is used to describe the included and parafoil body mass together. The 6-DOF equations of motion for the parafoil/payload body can be determined by solving the above dynamic equations in combination with the kinematic equations in (3.8) and (3.9).

The 7/8-DOF model's **L** matrix is partitioned into a block 4 x 5 matrix. The vector including state derivatives and constraints is 12 x 1 in both cases. The vector includes the seven dynamic state derivatives and five unknown constraints for the 7-DOF system and eight dynamic state derivatives and four unknown constraints for the 8-DOF system. The combined equations are formed in (3.63) for the 7-DOF model and (3.68) for the 8-DOF model, where the first and second row equations are found by summing the forces on the parafoil and payload, in their respective frames, and the third and fourth are obtained by summing the moments about parafoil and payload, also in their respective frames.

$$\begin{bmatrix} -m_s\mathbf{S}^{\mathbf{s}}_{\mathbf{r_{cs}}}\mathbf{K_1} & -m_s\mathbf{S}^{\mathbf{S}}_{\mathbf{r_{cS}}}\mathbf{K_2} & m_s\mathbf{T_{BS}} & -\mathbf{T_{BS}} & \mathbf{0_{3x2}} \\ \mathbf{0_{3x1}} & -m_{B+I}\mathbf{S}^{\mathbf{B}}_{\mathbf{r_{cB}}} - \mathbf{I}'_{\mathbf{AM}}\mathbf{S}^{\mathbf{B}}_{\mathbf{r_{cM}}} & m_{B+I}\mathbf{I_{3x3}} + \mathbf{I}'_{\mathbf{AM}} & \mathbf{I_{3x3}} & \mathbf{0_{3x2}} \\ \mathbf{I_S}\mathbf{K_1} & \mathbf{I_S}\mathbf{K_2} & \mathbf{0_{3x3}} & \mathbf{S}^{\mathbf{S}}_{\mathbf{r_{cS}}}\mathbf{T_{BS}} & -\mathbf{E_1} \\ \mathbf{0_{3x1}} & \mathbf{I_B} + \mathbf{I}'_{\mathbf{AI}} - \mathbf{S}^{\mathbf{B}}_{\mathbf{r_{BM}}}\mathbf{I}'_{\mathbf{AM}}\mathbf{S}^{\mathbf{B}}_{\mathbf{r_{cM}}} & \mathbf{S}^{\mathbf{B}}_{\mathbf{r_{BM}}}\mathbf{I}'_{\mathbf{Am}} & -\mathbf{S}^{\mathbf{B}}_{\mathbf{r_{CB}}} & \mathbf{T}^{T}_{\mathbf{BS}}\mathbf{E_1} \end{bmatrix} \begin{Bmatrix} \dot{r}_s \\ \cdots \\ \dot{p}_B \\ \dot{q}_B \\ \dot{r}_B \\ \cdots \\ \dot{u}_c \\ \dot{v}_c \\ \dot{w}_c \\ \cdots \\ F_{cx} \\ F_{cy} \\ F_{cz} \\ \cdots \\ M_{cx} \\ M_{cy} \end{Bmatrix} = \begin{Bmatrix} \mathbf{B_1} \\ \cdots \\ \mathbf{B_2} \\ \cdots \\ \mathbf{B_3} \\ \cdots \\ \mathbf{B_4} \end{Bmatrix}, \tag{3.63}$$

where

$$\mathbf{B_1} = \mathbf{F_S} + \mathbf{F_{W_S}} + \mathbf{m_S}\mathbf{S}^{\mathbf{s}}_{\mathbf{r_{cS}}}\mathbf{G} - \mathbf{m_S}\mathbf{S}^{\mathbf{S}}_{\boldsymbol{\omega}_\mathbf{S}}\mathbf{S}^{\mathbf{S}}_{\boldsymbol{\omega}_\mathbf{S}}\mathbf{r_{cS}} - \mathbf{m_S}\mathbf{T_{BS}}\mathbf{S}^{\mathbf{B}}_{\boldsymbol{\omega}_\mathbf{B}}\mathbf{V_c} \tag{3.64}$$

$$\begin{aligned} \mathbf{B_2} = \mathbf{F_A} + \mathbf{F_{W_B}} - m_{B+I}\mathbf{S}^{\mathbf{B}}_{\boldsymbol{\omega}_\mathbf{B}}\mathbf{V_c} - m_{B+I}\mathbf{S}^{\mathbf{B}}_{\boldsymbol{\omega}_\mathbf{B}}\mathbf{S}^{\mathbf{B}}_{\boldsymbol{\omega}_\mathbf{B}}\mathbf{r_{cB}} \\ - \mathbf{T_{BP}}^{\boldsymbol{T}}\mathbf{S}^{\mathbf{P}}_{\boldsymbol{\omega}_\mathbf{B}}\mathbf{I_{AM}}\widetilde{\mathbf{V}} - \mathbf{I}'_{\mathbf{AM}}\mathbf{S}^{\mathbf{B}}_{\boldsymbol{\omega}_\mathbf{B}}\mathbf{T_{IB}}\mathbf{V_{A/I}} \end{aligned} \tag{3.65}$$

$$\mathbf{B_3} = -\mathbf{I_S}\mathbf{G} - \mathbf{S}^{\mathbf{S}}_{\boldsymbol{\omega}_\mathbf{S}}\mathbf{I_S}\boldsymbol{\omega}_\mathbf{S} + \mathbf{T_{BS}}\begin{Bmatrix} 0 \\ 0 \\ M_{CZ} \end{Bmatrix} \tag{3.66}$$

$$\begin{aligned} \mathbf{B_4} = \mathbf{M_A} + \mathbf{S}^{\mathbf{B}}_{\mathbf{r_{BA}}}\mathbf{F_A} - \mathbf{S}^{\mathbf{B}}_{\mathbf{r_{BM}}}\mathbf{T_{BP}}^{\boldsymbol{T}}\mathbf{S}^{\mathbf{P}}_{\boldsymbol{\omega}_\mathbf{B}}\mathbf{I_{AM}}\widetilde{\mathbf{V}} - \begin{Bmatrix} 0 \\ 0 \\ M_{CZ} \end{Bmatrix} \\ - \mathbf{T_{BP}}^{\boldsymbol{T}}\mathbf{S}^{\mathbf{P}}_{\boldsymbol{\omega}_\mathbf{B}}\mathbf{I_{AI}}\widetilde{\boldsymbol{\omega}} - \mathbf{S}^{\mathbf{B}}_{\mathbf{r_{BM}}}\mathbf{I}'_{\mathbf{AM}}\mathbf{S}^{\mathbf{B}}_{\boldsymbol{\omega}_\mathbf{B}}\mathbf{T_{IB}}\mathbf{V_{A/I}} \\ - \mathbf{S}^{\mathbf{B}}_{\boldsymbol{\omega}_\mathbf{B}}\mathbf{I_B}\boldsymbol{\omega}_\mathbf{B} \end{aligned} \tag{3.67}$$

$$\begin{bmatrix} -m_s\mathbf{S}^{\mathbf{s}}_{\mathbf{r_{cs}}}\mathbf{K_1} & -m_s\mathbf{S}^{\mathbf{S}}_{\mathbf{r_{cS}}}\mathbf{K_2} & m_s\mathbf{T_{BS}} & -\mathbf{T_{BS}} & \mathbf{0_{3x1}} \\ \mathbf{0_{3x2}} & -\mathrm{m}_{\mathrm{B+I}}\mathbf{S}^{\mathbf{B}}_{\mathbf{r_{cB}}} - \mathbf{I}'_{\mathbf{AM}}\mathbf{S}^{\mathbf{B}}_{\mathbf{r_{cM}}} & m_{B+I}\mathbf{I_{3x3}} + \mathbf{I}'_{\mathbf{AM}} & \mathbf{I_{3x3}} & \mathbf{0_{3x1}} \\ \mathbf{I_S K_1} & \mathbf{I_S K_2} & \mathbf{0_{3x3}} & \mathbf{S}^{\mathbf{S}}_{\mathbf{r_{cS}}}\mathbf{T_{BS}} & -\mathbf{E_1} \\ \mathbf{0_{3x2}} & \mathbf{I_B} + \mathbf{I}'_{\mathbf{AI}} - \mathbf{S}^{\mathbf{B}}_{\mathbf{r_{BM}}}\mathbf{I}'_{\mathbf{AM}}\mathbf{S}^{\mathbf{B}}_{\mathbf{r_{cM}}} & \mathbf{S}^{\mathbf{B}}_{\mathbf{r_{BM}}}\mathbf{I}'_{\mathbf{AM}} & -\mathbf{S}^{\mathbf{B}}_{\mathbf{r_{CB}}} & \mathbf{T_{BS}}^{T}\mathbf{E_1} \end{bmatrix} \begin{Bmatrix} \dot{q}_S \\ \dot{r}_S \\ \cdots \\ \dot{p}_B \\ \dot{q}_B \\ \dot{r}_B \\ \cdots \\ \dot{u}_c \\ \dot{v}_c \\ \dot{w}_c \\ \cdots \\ F_{cx} \\ F_{cy} \\ F_{cz} \\ \cdots \\ M_{cy} \end{Bmatrix} = \begin{Bmatrix} \mathbf{B_1} \\ \cdots \\ \mathbf{B_2} \\ \cdots \\ \mathbf{B_3} \\ \cdots \\ \mathbf{B_4} \end{Bmatrix}, \tag{3.68}$$

where

$$\mathbf{B_1} = \mathbf{F_S} + \mathbf{F_{W_S}} + m_S\mathbf{S}^{\mathbf{s}}_{\mathbf{r_{CS}}}\mathbf{G} - m_S\mathbf{S}^{\mathbf{S}}_{\boldsymbol{\omega}_{\mathbf{S}}}\mathbf{S}^{\mathbf{S}}_{\boldsymbol{\omega}_{\mathbf{S}}}\mathbf{r_{CS}} - m_S\mathbf{T_{BS}}\mathbf{S}^{\mathbf{B}}_{\boldsymbol{\omega}_{\mathbf{B}}}\mathbf{V_C} \tag{3.69}$$

$$\begin{aligned} \mathbf{B_2} = \mathbf{F_A} + \mathbf{F_{W_B}} - m_{B+I}\mathbf{S}^{\mathbf{B}}_{\boldsymbol{\omega}_{\mathbf{B}}}\mathbf{V_C} - m_{B+I}\mathbf{S}^{\mathbf{B}}_{\boldsymbol{\omega}_{\mathbf{B}}}\mathbf{S}^{\mathbf{B}}_{\boldsymbol{\omega}_{\mathbf{B}}}\mathbf{r_{CB}} \\ - \mathbf{T_{BP}}^{T}\mathbf{S}^{\mathbf{P}}_{\boldsymbol{\omega}_{\mathbf{B}}}\mathbf{I_{AM}}\widetilde{\mathbf{V}} - \mathbf{I}'_{\mathbf{AM}}\mathbf{S}^{\mathbf{B}}_{\boldsymbol{\omega}_{\mathbf{B}}}\mathbf{T_{IB}}\mathbf{V_{A/I}} \end{aligned} \tag{3.70}$$

$$\mathbf{B_3} = -\mathbf{I_S G} - \mathbf{S}^{\mathbf{S}}_{\boldsymbol{\omega}_{\mathbf{S}}}\mathbf{I_S}\boldsymbol{\omega}_{\mathbf{S}} + \mathbf{T_{BS}}\begin{Bmatrix} 0 \\ M_{cy} \\ M_{cz} \end{Bmatrix} \tag{3.71}$$

$$\begin{aligned} \mathbf{B_4} = \mathbf{M_A} + \mathbf{S}^{\mathbf{B}}_{\mathbf{r_{BA}}}\mathbf{F_A} - \mathbf{S}^{\mathbf{B}}_{\mathbf{r_{BM}}}\mathbf{T_{BP}}^{T}\mathbf{S}^{\mathbf{P}}_{\boldsymbol{\omega}_{\mathbf{B}}}\mathbf{I_{AM}}\widetilde{\mathbf{V}} - \begin{Bmatrix} 0 \\ M_{cy} \\ M_{cz} \end{Bmatrix} - \\ \mathbf{T_{BP}}^{T}\mathbf{S}^{\mathbf{P}}_{\boldsymbol{\omega}_{\mathbf{B}}}\mathbf{I_{AI}}\widetilde{\boldsymbol{V}} - \mathbf{S}^{\mathbf{B}}_{\mathbf{r_{BM}}}\mathbf{I}'_{\mathbf{AM}}\mathbf{S}^{\mathbf{B}}_{\boldsymbol{\omega}_{\mathbf{B}}}\mathbf{T_{IB}}\mathbf{V_{A/I}} - \mathbf{S}^{\mathbf{B}}_{\boldsymbol{\omega}_{\mathbf{B}}}\mathbf{I_B}\boldsymbol{\omega}_{\mathbf{B}}. \end{aligned} \tag{3.72}$$

The 7-DOF equations of motion for the parafoil/payload body can be determined by solving the above dynamic equations (3.63-3.67) in combination with the kinematic equations in (3.8), (3.9), and (3.19). The 8-DOF equations of motion for the parafoil/payload body can be determined by solving the above dynamic equations (3.68-3.72) in combination with the kinematic equations in (3.8), (3.9), and (3.20).

The payload is allowed to rotate freely in the 9-DOF system therefore the internal constraint moments are absent. The **L** matrix is partitioned into a block 4 x 4 matrix and the vector to be solved includes twelve state derivatives. The dynamic equations are provide in (3.73-3.77). As with the 7- and 8- DOF models, the first and second row equations are found by summing the forces on the parafoil and payload in their respective frames, and the third and fourth are obtained by summing the moments about parafoil and payload mass centers, in their respective frames.

$$\begin{bmatrix} -m_S\mathbf{S}^{\mathbf{S}}_{\mathbf{r_{cs}}} & \mathbf{0_{3x3}} & m_S\mathbf{T_{BS}} & -\mathbf{T_{BS}} \\ \mathbf{0_{3x3}} & -m_{B+I}\mathbf{S}^{\mathbf{B}}_{\mathbf{r_{cB}}} - \mathbf{I}'_{\mathbf{AM}}\mathbf{S}^{\mathbf{B}}_{\mathbf{r_{cM}}} & m_{B+I}\mathbf{I_{3x3}} + \mathbf{I}'_{\mathbf{AM}} & \mathbf{I_{3x3}} \\ \mathbf{I_S} & \mathbf{0_{3x3}} & \mathbf{0_{3x3}} & \mathbf{S}^{\mathbf{S}}_{\mathbf{r_{cS}}}\mathbf{T_{BS}} \\ \mathbf{0_{3x3}} & \mathbf{I_B} + \mathbf{I}'_{\mathbf{AI}} - \mathbf{S}^{\mathbf{B}}_{\mathbf{r_{BM}}}\mathbf{I}'_{\mathbf{AM}}\mathbf{S}^{\mathbf{B}}_{\mathbf{r_{cM}}} & \mathbf{S}^{\mathbf{B}}_{\mathbf{r_{BM}}}\mathbf{I}'_{\mathbf{AM}} & -\mathbf{S}^{\mathbf{B}}_{\mathbf{r_{CB}}} \end{bmatrix} \begin{Bmatrix} \dot{p}_S \\ \dot{q}_S \\ \dot{r}_S \\ \cdots \\ \dot{p}_B \\ \dot{q}_B \\ \dot{r}_B \\ \cdots \\ \dot{u}_c \\ \dot{v}_c \\ \dot{w}_c \\ \cdots \\ F_{cx} \\ F_{cy} \\ F_{cz} \end{Bmatrix} = \begin{Bmatrix} \mathbf{B_1} \\ \cdots \\ \mathbf{B_2} \\ \cdots \\ \mathbf{B_3} \\ \cdots \\ \mathbf{B_4} \end{Bmatrix}, \tag{3.73}$$

where

$$\mathbf{B_1} = \mathbf{F_S} + \mathbf{F_{W_S}} - m_S\mathbf{S}^{\mathbf{S}}_{\boldsymbol{\omega}_\mathbf{S}}\mathbf{S}^{\mathbf{S}}_{\boldsymbol{\omega}_\mathbf{S}}\mathbf{r_{cS}} - m_S\mathbf{T_{BS}}\mathbf{S}^{\mathbf{B}}_{\boldsymbol{\omega}_\mathbf{B}}\mathbf{V_c} \tag{3.74}$$

$$\mathbf{B_2} = \mathbf{F_A} + \mathbf{F_{W_B}} + m_{B+I}\mathbf{S^B_{\omega_B}V_c} - m_{B+I}\mathbf{S^B_{\omega_B}S^B_{\omega_B}r_{cB}} - \mathbf{T_{BP}}^T\mathbf{S^P_{\omega_B}I_{AM}\tilde{V}} - \mathbf{I'_{AM}S^B_{\omega_B}T_{IB}V_{A/I}} \tag{3.75}$$

$$\mathbf{B_3} = \mathbf{M_c} - \mathbf{S^S_{\omega_S}I_S\omega_S} \tag{3.76}$$

$$\mathbf{B_4} = \mathbf{M_A} + \mathbf{S^B_{r_{BA}}F_A} - \mathbf{S^B_{r_{BM}}T_{BP}}^T\mathbf{S^P_{\omega_B}I_{AM}\tilde{V}} - \mathbf{M_c} - \mathbf{T_{BP}}^T\mathbf{S^P_{\omega_B}I_{AI}\tilde{\omega}} - \mathbf{S^B_{r_{BM}}I'_{AM}S^B_{\omega_B}T_{IB}V_{A/I}} - \mathbf{S^B_{\omega_B}I_B\omega_B}. \tag{3.77}$$

The 9-DOF equations of motion for the parafoil/payload body can be determined by solving the above dynamic equations in combination with the kinematic equations in (3.8), (3.9), and (3.15).

CHAPTER 4

EXPERIMENTAL PLATFORM

4.1 Miniature Parafoil-Payload

The deployed experimental parafoil system is shown in Figure 4.1 and is similar to the system used in [13] and [14]. The payload is rectangular with a drag area of 0.45 ft^2 a depth of 0.4 ft, has a weight of 4.23 lbf, and contains the flight computer and all auxiliary electronics. The parafoil canopy and suspension lines have a combined weight of 0.45 lbf. The 7-cell canopy has a span of 4.25 ft, mean chord of 2.5 ft, Γ of -12 degrees, and maximum control deflection of 0.75 ft.

Figure 4.1 Parafoil-payload test platform.

Connection of the parafoil canopy and payload is achieved through a four point riser connection as shown in Figure 4.2. The geometry of the four connection points can significantly alter the relative motion between the parafoil canopy and payload. If all four connections coincide at the center then an ideal confluence point of the 9 DOF model is closely represented.

In contrast, if the width and length of the connections are sufficiently large, then no significant payload relative yaw, pitch or roll is allowed unless the risers, twist, stretch or become slack and the 6-DOF model connection is closely approximated. When connection distances are moderate, the payload may be able to twist about its vertical axis without risers stretching or becoming slack and an ideal 7-DOF model with only relative parafoil-payload twist is closely represented.

If the connections coincide as two pairs, with no separation in either the fore-aft or left-right direction, connections mimicking free pitching or rolling are created, respectively. Such configurations are represented by 8-DOF models which include relative twist and relative pitch.

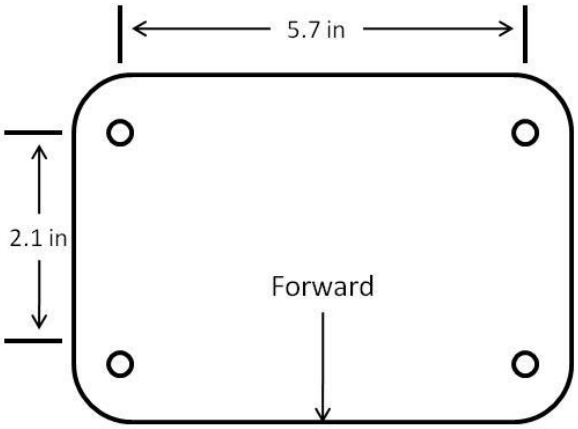

Figure 4.2 Payload top view showing connection points.

Inspection of the experimental riser connection demonstrates that none of the ideal confluence configurations are represented. While connections are as far apart as physically possible they are still relatively close. The experimental configuration was chosen because it achieved a high level of restriction to parafoil-payload relative motion for the system. In general, modelers could reasonably justify any of the models ranging from 6 to 9-DOF.

The entire sensor system is made up of two components; the first is the main flight computer in Figure 4.3 and the second will be discussed in more detail in the next section. The flight computer attaches to a main sensor board which includes three accelerometers, gyroscopes and magnetometers, a global positioning system (GPS), barometric altimeter, mid-range wireless transceiver and ultra low power transceiver.

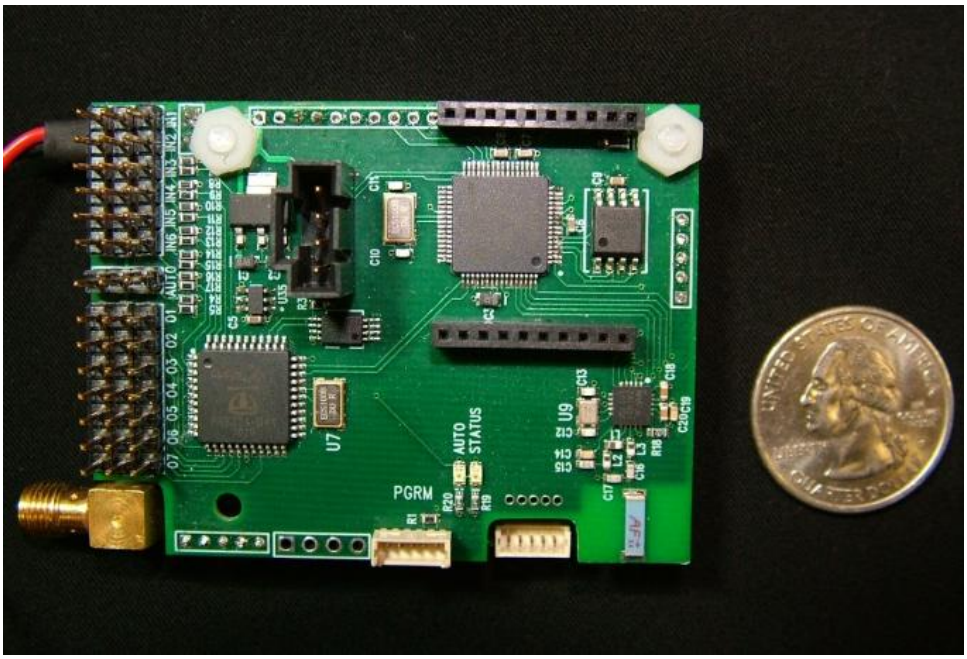

Figure 4.3 Flight computer.

Figure 4.4 Payload container.

The navigation box, Figure 4.4, contains the flight computer with sensor board, external memory, servos and controllers. The control lines are connected to winches (mechanical device that increase or decrease the length of the line) that control the canopy yaw angle. To bank right, the winches decrease the length of the right control line. Similarly, to bank left, the length of the left control line is decrease while the right remains constant.

4.2 Bantam Sensor Board

The second component is the developed Bantam sensor which was created to measure parafoil-payload motion without interfering with general operations. The Bantam is 1.7 in^2; roughly the size of a US quarter, and weighs about 0.02 lbs including the battery, which is less than the weight of two quarters. The board is fitted with a 32-bit microprocessor, temperature sensor, three gyroscopes, three accelerometers, three magnetometers, and a low power wireless transceiver with 65 ft range.

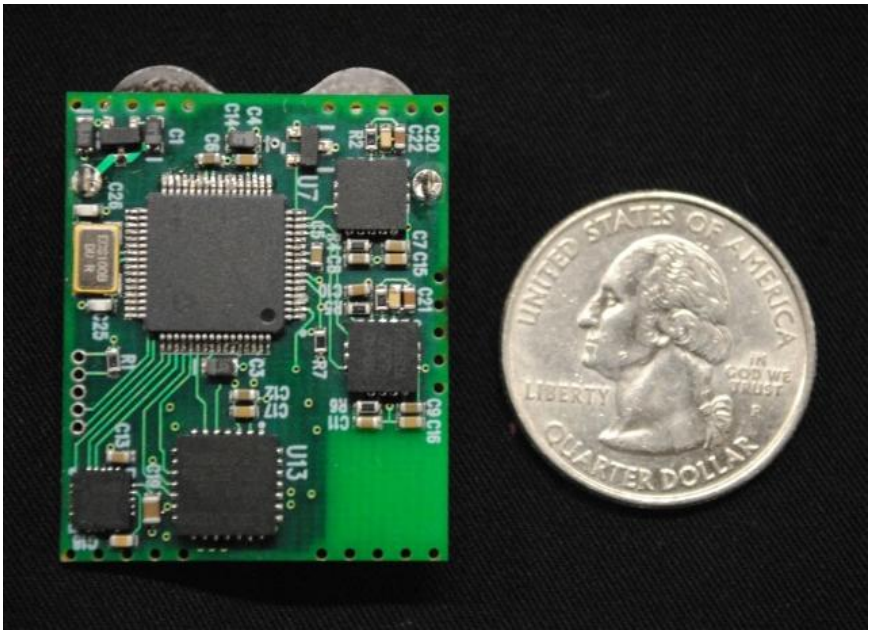

Figure 4.5 Bantam sensor board.

The Bantam has two modes, online and sleep. In the online mode, the sensor calculates orientation and temperature compensated data at 100 Hz. In sleep mode the system maintains an ultra-low power state waiting for a prompt from the flight computer which then initiates online mode. The battery life of the sensor while sleeping is about 12-36 hours depending on the desired sensor activation response time which allows the system to be packed in the canopy overnight. When the sensor is fully online, the Bantam

can run continuously for about 2 hours. The Bantam has the same inertial sensors and ultra-low power wireless transceiver as the Flight computer.

The Bantam sensors were sewn to the canopy inside the cells as seen in Figure 4.6 using small holes around the sensor edge visible in Figure 4.5.

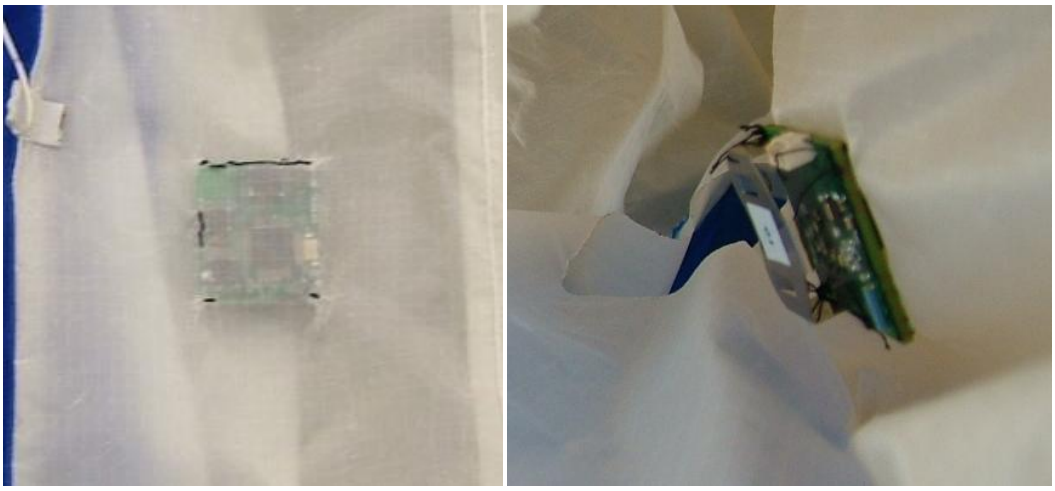

Figure 4.6 Bantam sensor in canopy.

Two Bantam sensors were placed inside cells three and five at a quarter chord of canopy, 0.89 ft away from the canopy centerline as shown in Figure 4.7. This setup provided the ability to measure canopy movement in port and starboard sides and redundancy for robustness.

Figure 4.7 Location of Bantam sensors in canopy.

CHAPTER 5

RESULTS

5.1 Simulation Results

5.1.1 Initial Conditions and Model Variables

The 6/7/8/9-DOF models are numerically integrated using a fourth order Runge-Kutta algorithm with time step of 0.01 seconds. Flight test initial conditions and the miniature parafoil system discussed in the previous section were employed in the simulation. The simulation is started at zero cross range and down range, from 1300 ft above sea level, with payload and parafoil pitch angles of -0.50 degrees and 1.7 degrees, respectively, the velocity components are u_C being 25.71 ft/s, w_C being 13.62 ft/s, and all other states zero. The payload was also described in Chapter 4 and its measurements are used in the simulation. All aerodynamic coefficients and apparent mass coefficients for the canopy are provided in Table 5.1 [11, 18].

Table 5.1. Parafoil and Payload Physical Parameters

Parameter	Value	Units	Parameter	Value	Units
C_{D0}	0.15	-	C_{nr}	-0.02	-
$C_{D\alpha^2}$	0.90	-	$C_{n\delta a}$	0.004	-
$C_{Y\beta}$	-0.15	-	C_{DS}	0.40	-
C_{L0}	0.25	-	A	0.00084	$slug$
$C_{L\alpha}$	0.68	-	B	0.0022	$slug$
C_{lp}	-0.355	-	C	0.0290	$slug$
$C_{l\delta a}$	–0.00032	-	P	0.040	$slug \cdot ft^2$
C_{m0}	0.0	-	Q	0.010	$slug \cdot ft^2$
C_{mq}	-0.265	-	R	0.0018	$slug \cdot ft^2$

Inertia matrices for both the parafoil and payload are provided below with both having units of slug-ft^2.

$$\mathbf{I_B} = \begin{bmatrix} 0.031 & 0 & -0.005 \\ 0 & 0.020 & 0 \\ -0.005 & 0 & 0.040 \end{bmatrix} \tag{5.1}$$

$$\mathbf{I_S} = \begin{bmatrix} 0.0075 & 0 & 0 \\ 0 & 0.00675 & 0 \\ 0 & 0 & 0.0051 \end{bmatrix}. \tag{5.2}$$

Vectors from the point *C* to the payload mass center, parafoil mass center, and canopy rotation point are $\mathbf{r_{CS}}$ =0.3 $\mathbf{i_S}$ ft, $\mathbf{r_{CB}}$ =0.5 $\mathbf{i_B}$ - 2.25 $\mathbf{k_B}$ ft, and $\mathbf{r_{CR}}$ = -0.5 $\mathbf{i_B}$ - 2.7 $\mathbf{k_B}$ ft. Vectors from the canopy rotation point to the parafoil aerodynamic center and apparent mass center are $\mathbf{r_{RP}}$ =0.33 $\mathbf{i_P}$ ft and $\mathbf{r_{RM}}$ =0.59 $\mathbf{i_P}$ + 0.2 $\mathbf{k_P}$ ft, respectively. The rotational stiffness and damping from risers are assumed to be constant with values of 0.19 lbf-ft/rad and 0.0 lbf-ft-s/rad.

5.1.2 Simulation in MatLab

The simulation run in MatLab was similar to the situation experienced by the parafoil/payload body in the flight test with a series of 44% left and right brake deflection as shown in Figure 5.1. The resulting trajectory is a maneuver shown in Figure 5.2. The ground track illustrates the slight difference between the 6/7-DOF and the 8/9-DOF model trajectory. For the test system, relative payload motion displays little effect on the trajectory.

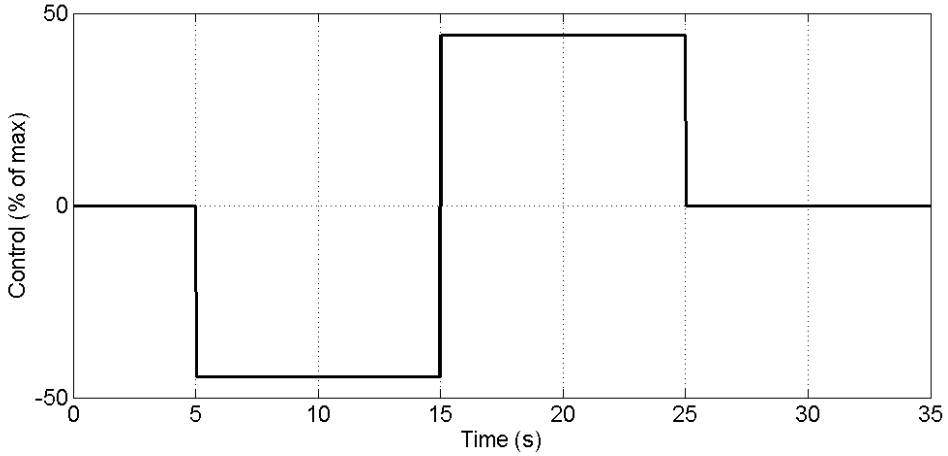

Figure 5.1 Brake deflection.

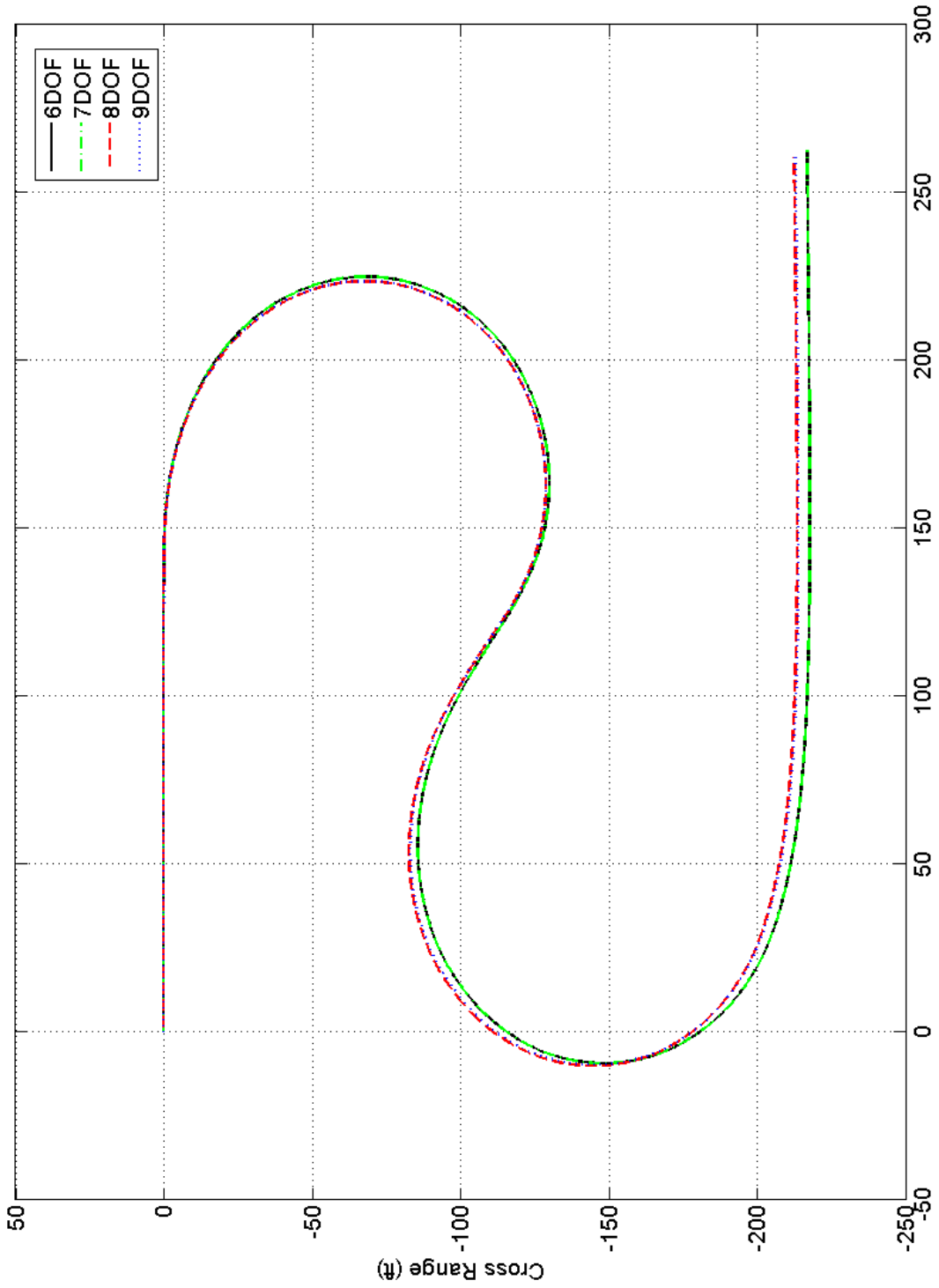

Figure 5.2 Ground track comparison.

Figures 5.3-5.5 show angular rates of the 6/7/8/9-DOF system for the parafoil and payload. Each figure is divided into three plots. The first plot is the 6-DOF motion while the second plot is the difference between the 6-DOF parafoil motion and that of the 7/8/9-DOF parafoil motion. The third plot is the relative motion of the payload with respect to the parafoil.

In Figure 5.3, the parafoil yaw rate oscillates at a significantly lower magnitude than the payload yaw rate. The parafoil steady state yaw rate is equivalent; however, the yaw rate for the 6-DOF which does not take into account relative payload yaw rate has substantially lower motion. For parafoil and payload pitch rate in Figure 5.4, the 7/8/9-DOF models show only small differences when compared to the 6-DOF model. It can be observed, since the 7-DOF model does not include relative payload pitch, the difference in trajectories are due to yaw roll coupling excited by the relative payload yawing. Similar to the pitch rate, payload roll rate in Figure 5.5, is very similar for the 7/8/9 DOF models. Difference between 6/7- and 8/9-DOF models are small and generated mainly from the coupling of relative yawing motion of the payload.

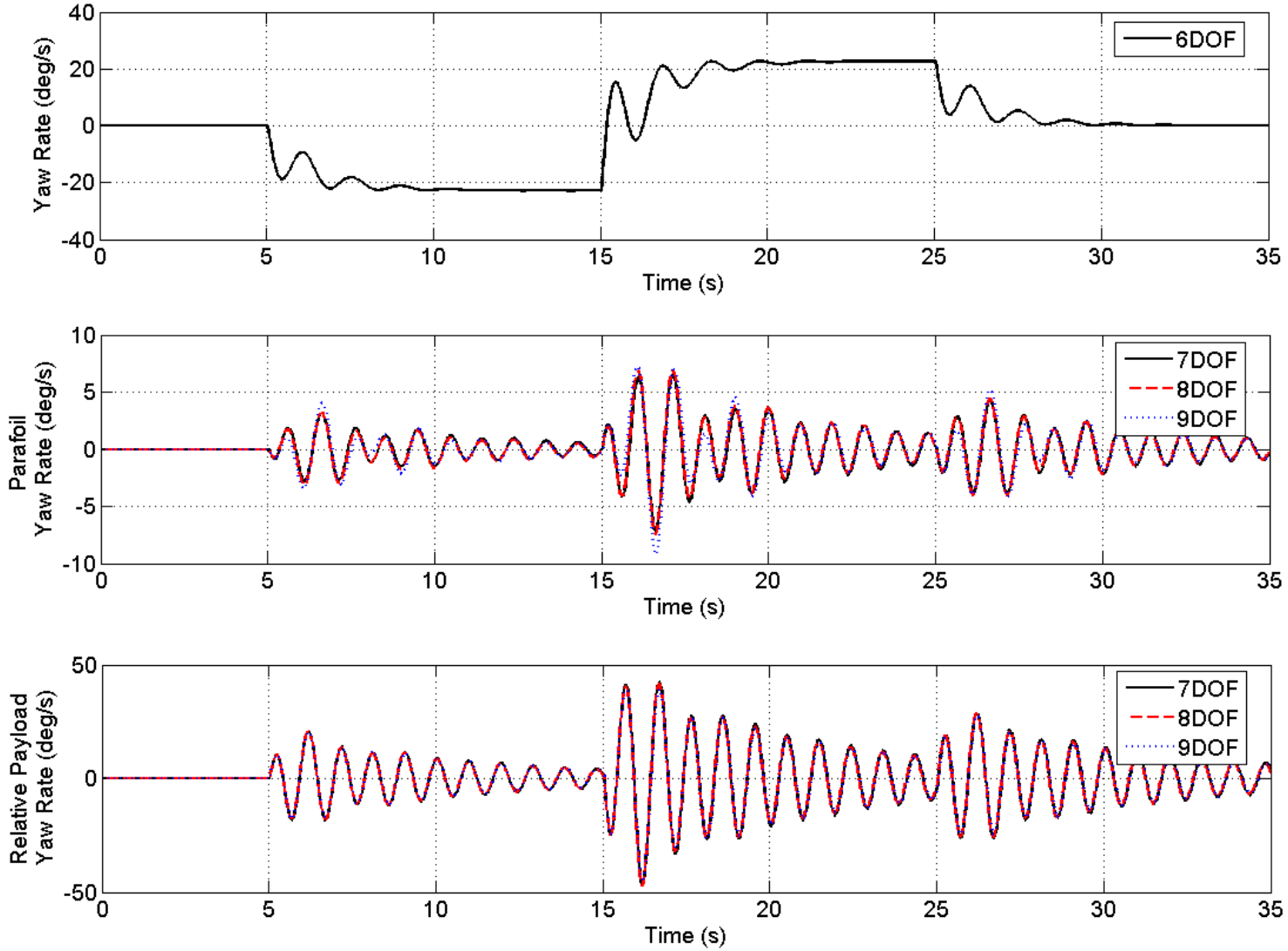

Figure 5.3 Parafoil and payload yaw rate.

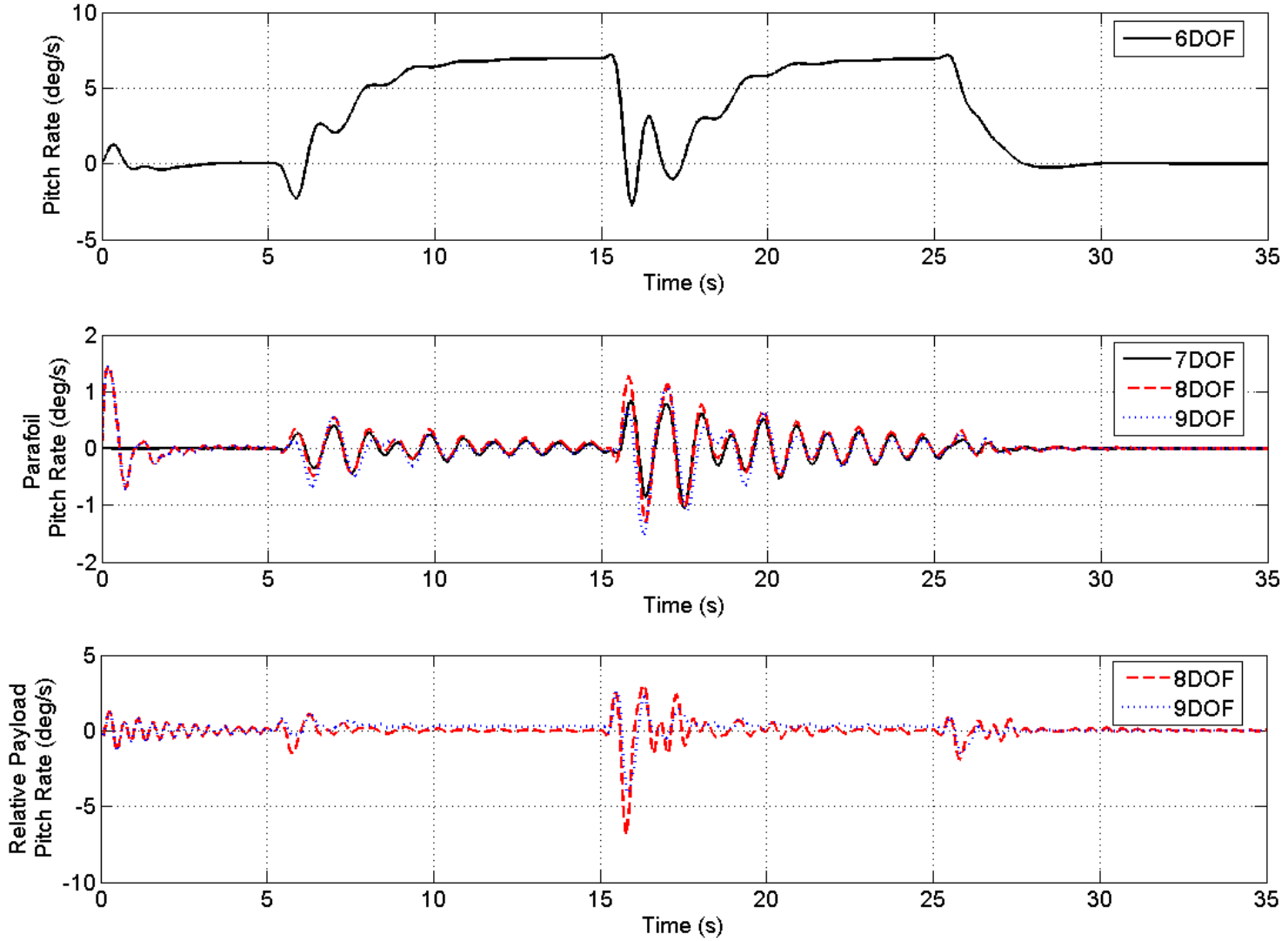

Figure 5.4 Parafoil and payload pitch rate.

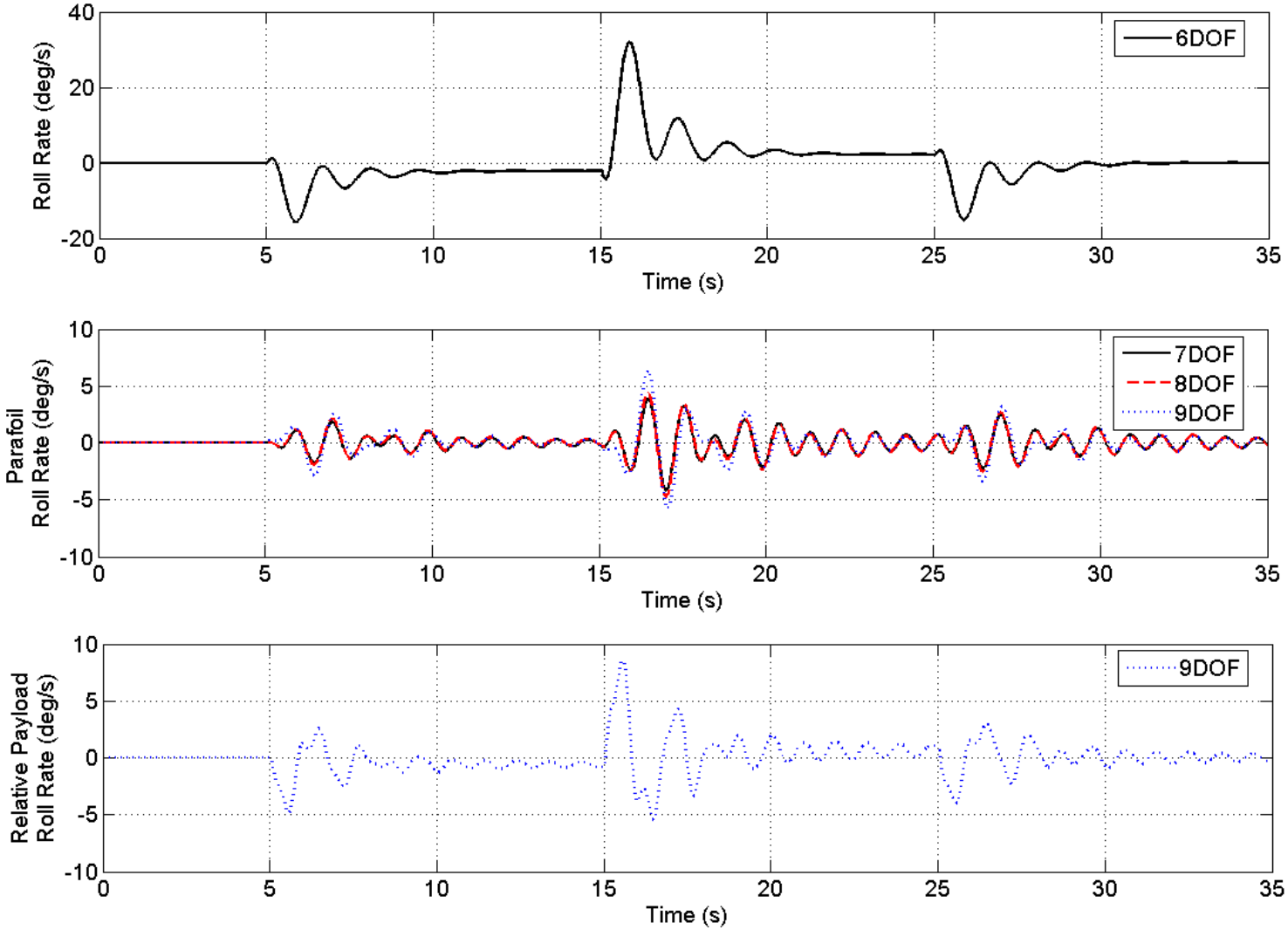

Figure 5.5 Parafoil and payload roll rate.

The following figures illustrate simulated Euler angles of the parafoil and payload. In Figure 5.6, difference between 6 and 7/8/9 DOF model yaw angles are slight. Minimal variations in the 7/8/9-DOF models indicate that all can accurately represent relative parafoil-payload twist and relative pitch and roll are not significantly couple to payload yaw. The payload yaw has oscillations that are about 4 times the magnitude of the parafoil oscillations. If payload sensors are used for control, this difference can generate changes in the close loop turn trajectory. Figure 5.7 shows that the differences between pitch in the models are small. Ability of the payload to pitch with respect to the canopy, however, allows a slight variation in the steady state pitch of the canopy in the 8/9-DOF models. Roll in Figure 5.8 similarly shows negligible variations in the parafoil while allowing the payload to remain closer to vertical during the turns.

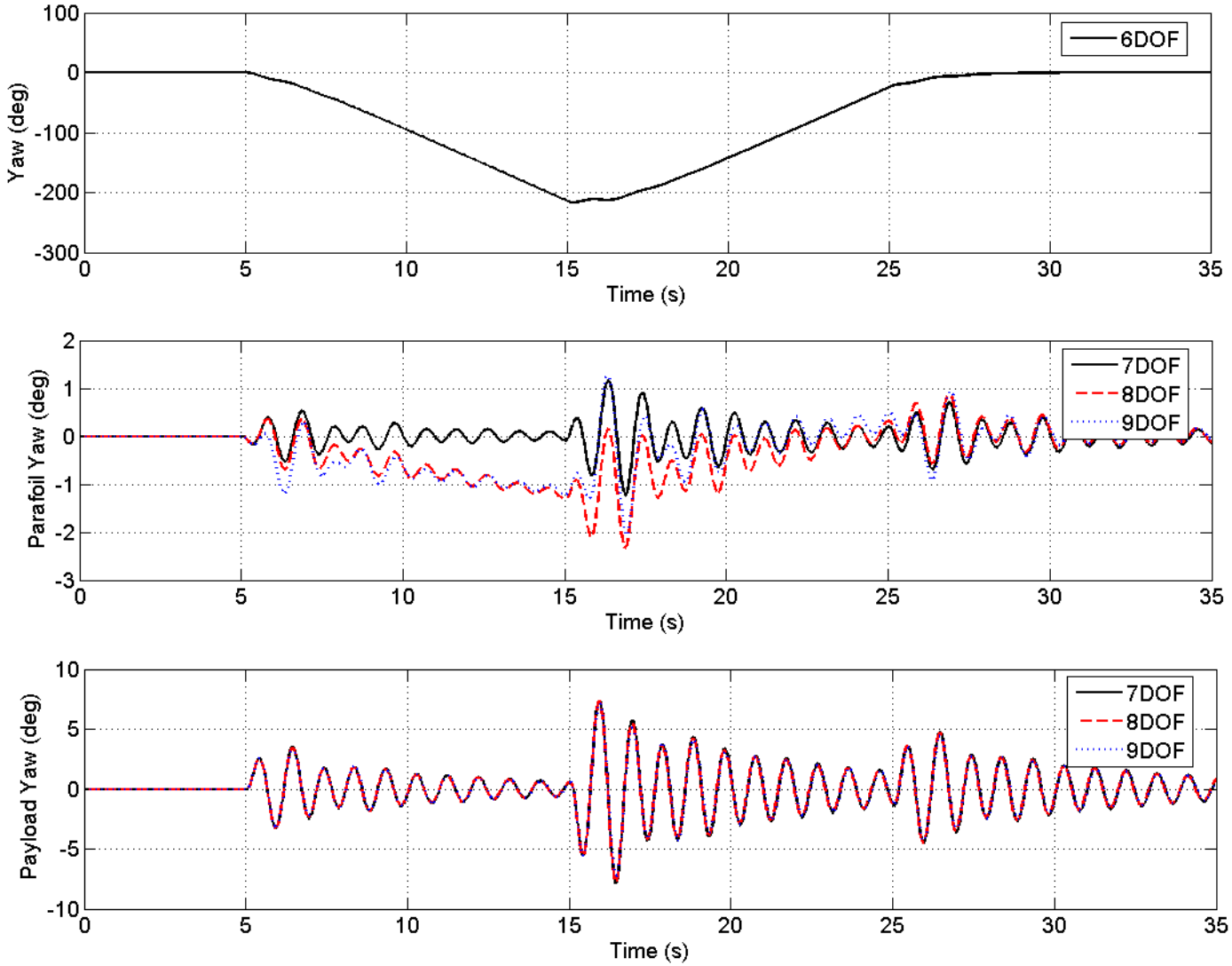

Figure 5.6 Parafoil and payload yaw.

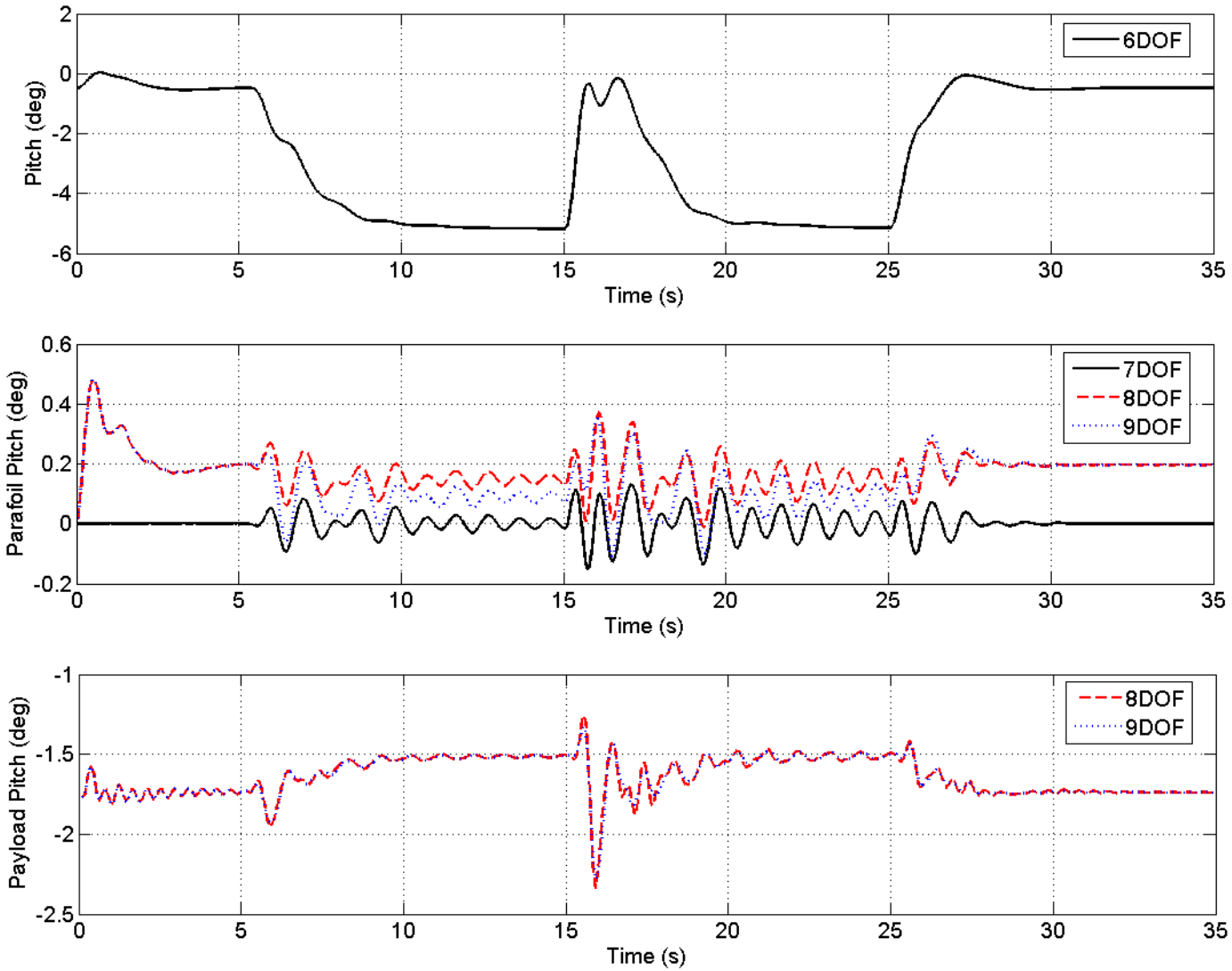

Figure 5.7 Parafoil and payload pitch.

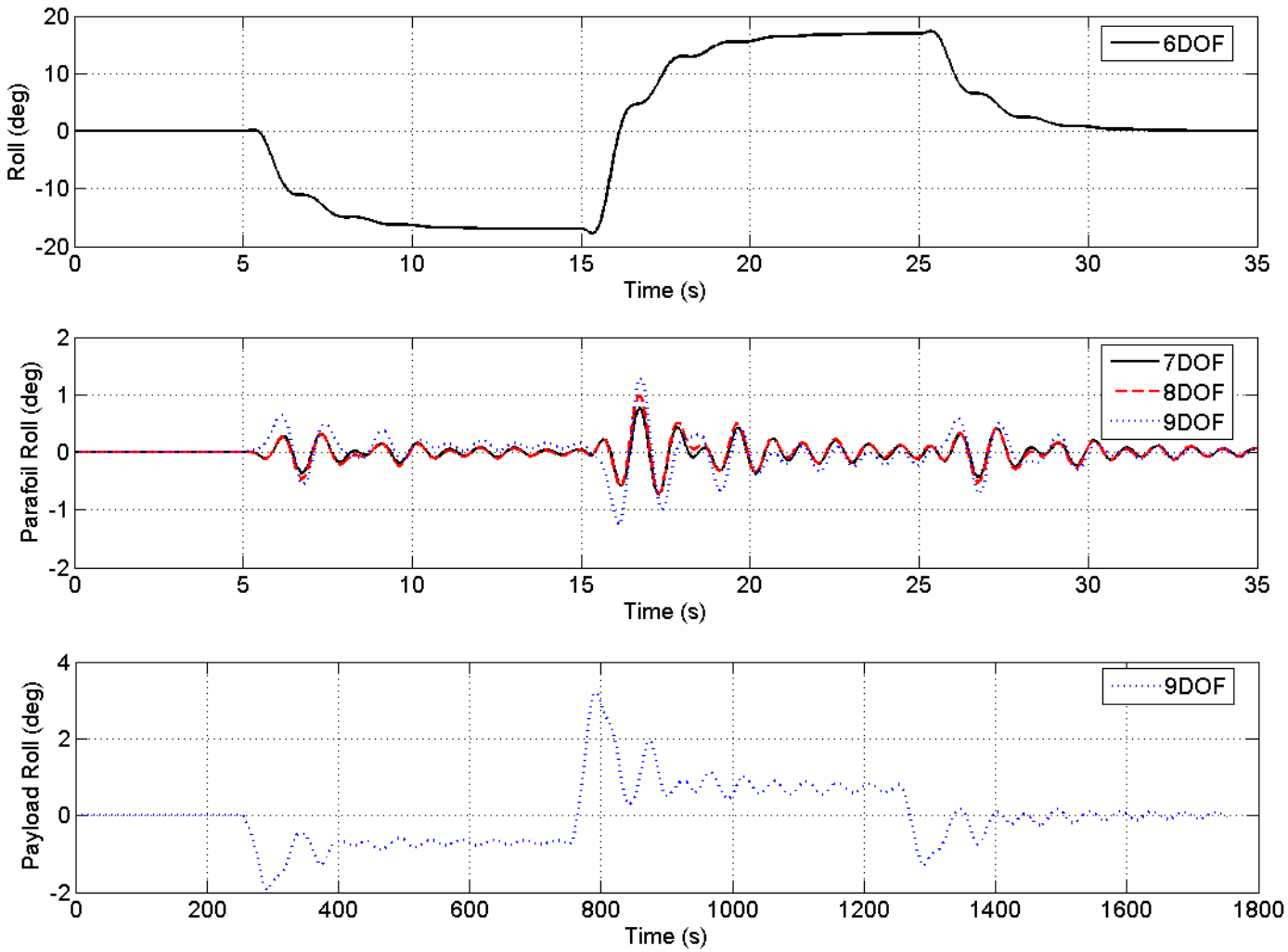

Figure 5.8 Parafoil and payload roll.

5.1.3 Large Payload Inertia Case

Generally, a canopy carries a payload that is much more massive than the canopy. For instance, the Joint Precision Airdrop (JPADS) Mega-fly, Figure 5.9, carries up to a 30,000 lbs payload which can twist freely. The dynamics of a system with a larger payload and different configuration would change the trajectory more than that of the test system discussed in Chapter 4.

Figure 5.9 JPADS MegaFly [23].

To simulate a larger freely twisting payload, the inertia component I_{zz} is increased by a factor of twenty while all other components remain the same. Also, the spring constant K_{ψ} which is used to represent the twist in the lines, is set to zero.

Figure 5.10 shows the cross range of a system with a large freely twisting payload. The 6-DOF trajectory is significantly different from the 7/8/9-DOF model trajectory. Since the 7/8/9-DOF model trajectories are similar, the 7-DOF could then be assumed to include the minimum number of degrees of freedom to capture important motion.

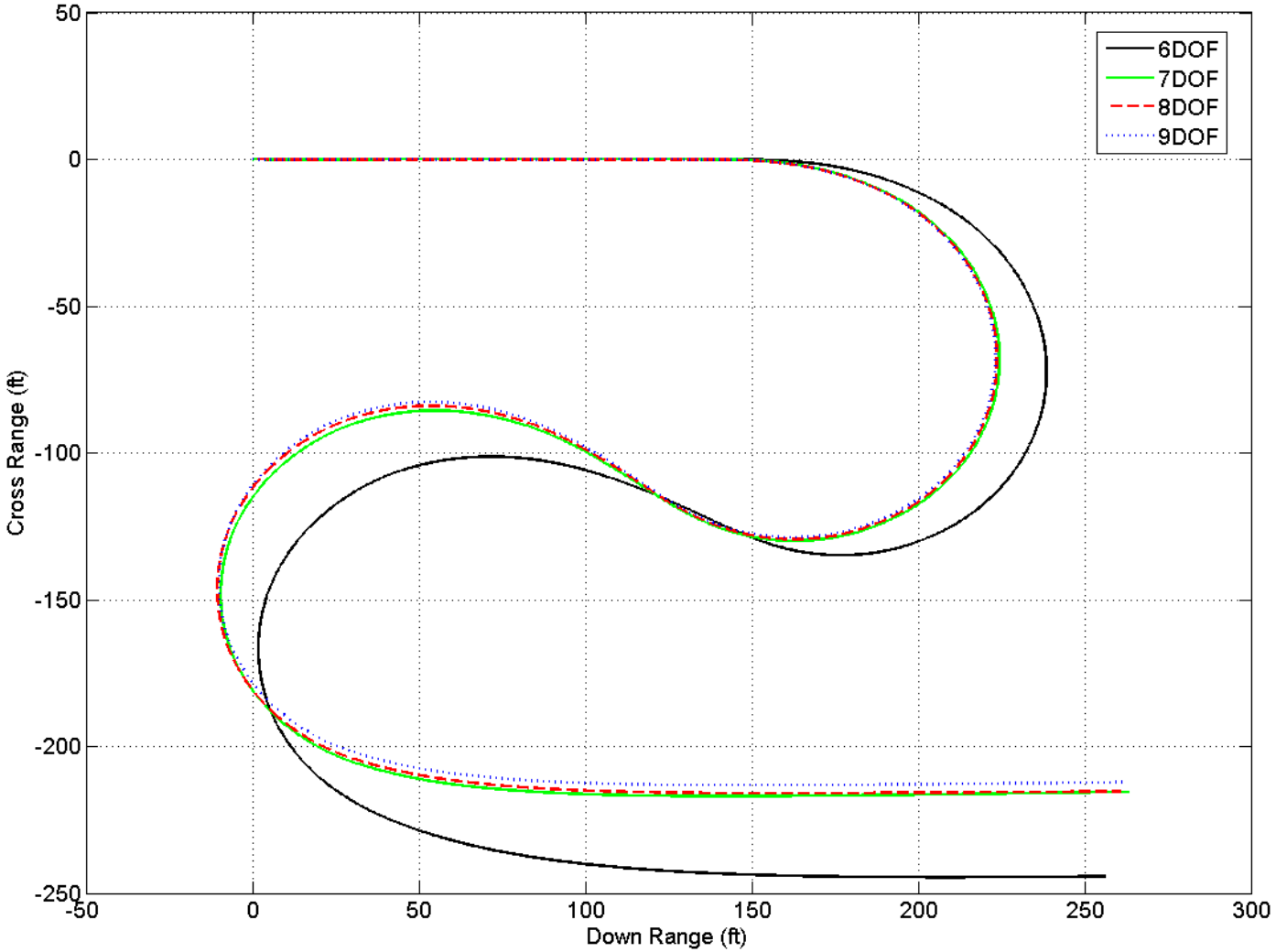

Figure 5.10 Cross range of a system with a larger freely twisting payload.

In further detail, the first brake deflection is displayed in Figure 5.11 which illustrates the difference in yaw and yaw rates that cause the divergence between the 6- and 7-DOF trajectories. The steady state turn angle for 6-DOF lags behind the 7-DOF and by the second maneuver is 20.4° offset. This effect can also be seen in the yaw rate, where the 7-DOF increases faster than the 6-DOF but both reach the same steady state turn rate. Figure 5.12 demonstrates the correlation between steady state turn lag and the inertia ratio of the parafoil and payload which is a linear trend with a slope of 5.2 deg. The inertia ratio can be found by

$$\text{Inertia Ratio} = \frac{I_{zz_S}}{\left(I_{zz_B}+C\right)}. \tag{5.1}$$

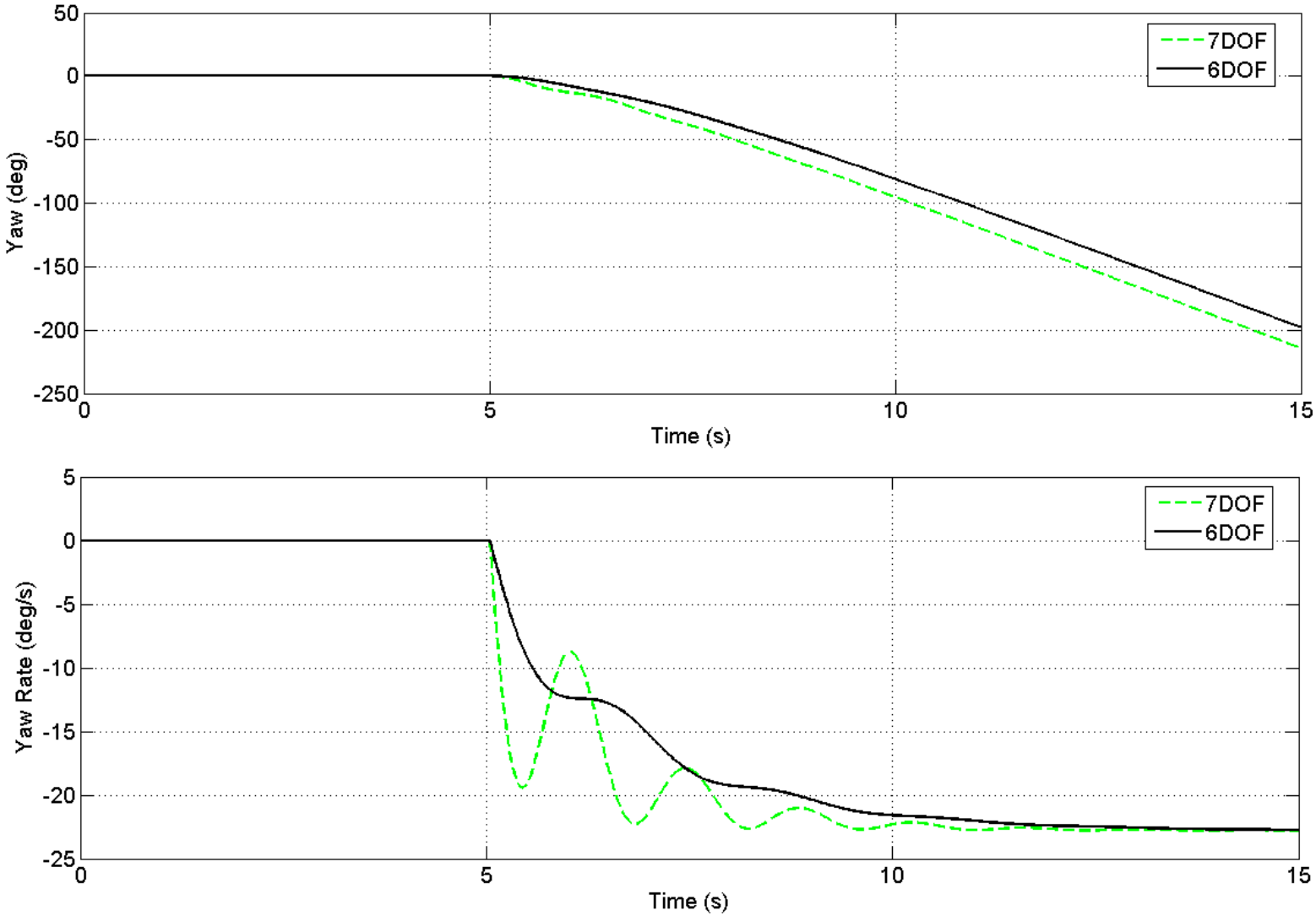

Figure 5.11 Yaw and yaw rate of a system with a larger freely twisting payload.

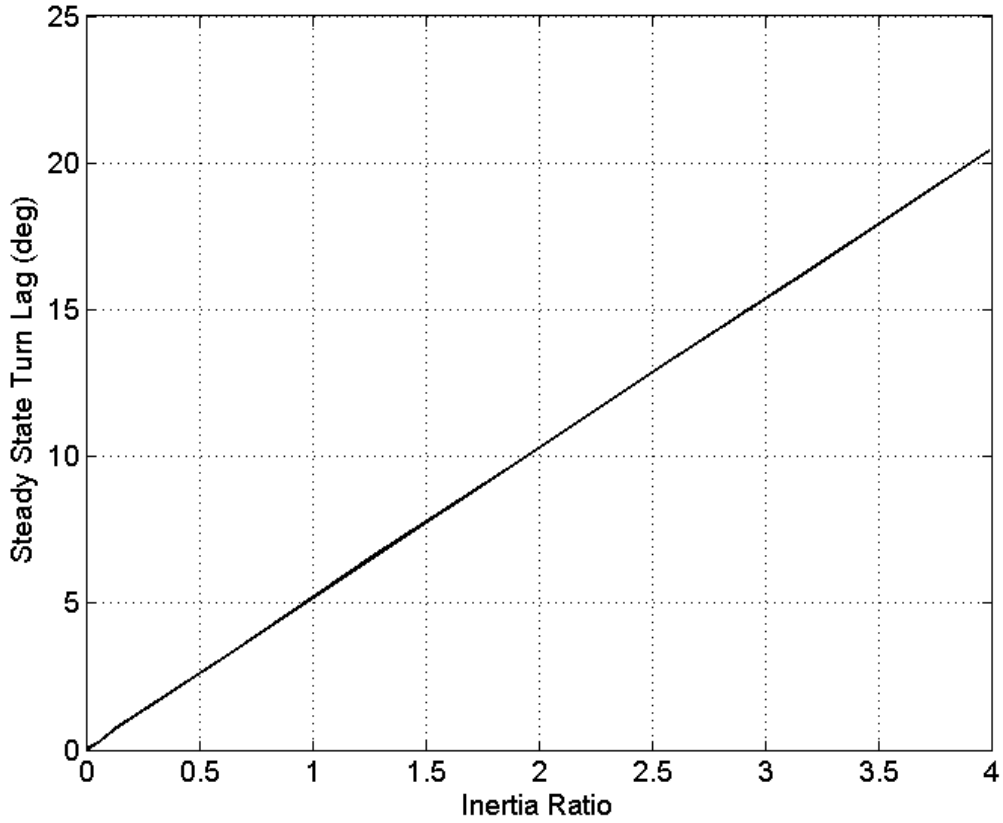

Figure 5.12 Steady state turn lag vs. inertia ratio.

5.2 Experimental Results

5.2.1 Experimental Initial Conditions

The experimental parafoil system was released from an altitude of 1300 ft and data was recorded from both canopy sensors and the payload at 12 Hz. During the approximately 80 seconds before touch down, a series of left and right turns was made using brake deflections ranging from 40% to 60% of the maximum range.

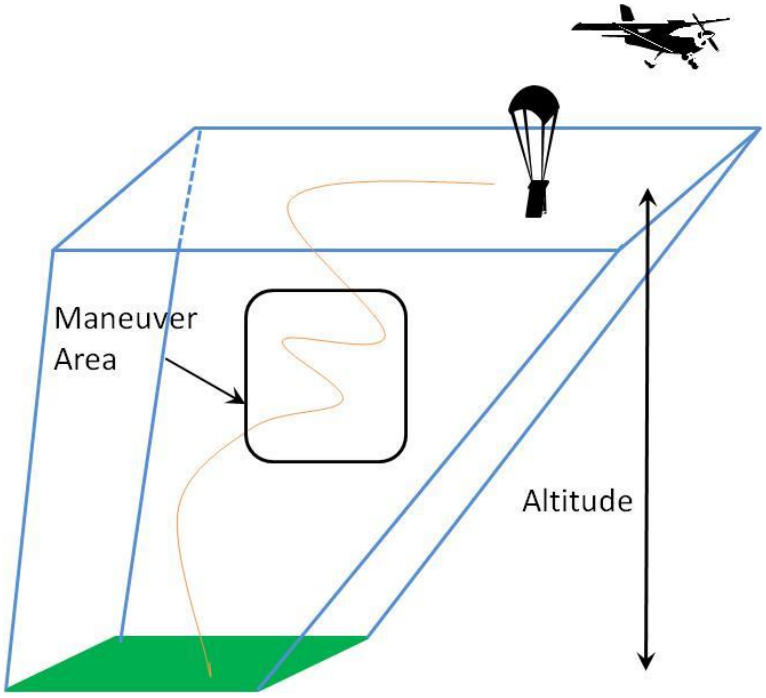

Figure 5.13 Experimental test parameters.

5.2.2 Model Frequencies

Figures 5.14 and 5.15 show the amplitude spectrum of measured angular velocities for both the payload and parafoil canopy, respectively. From Figure 5.14, it is observed that the payload roll and pitch rate amplitude spectrums have similar components at 2.1 Hz and 2.2 Hz. The payload yaw rate has two components, a low frequency component at 0.05 Hz from the control input, and a dynamic twisting mode at 1.05 Hz. The angular velocity amplitude spectrum for the total canopy is found by combining data

from both canopy sensors into one signal representing the average canopy motion. The canopy pitch rate amplitude spectrum in Figure 5.15 has a peak at 2.2 Hz, near that of the payload pitch rate but of lesser magnitude and is a result of the two body's pitch coupling. Both the canopy roll and yaw rates have a significant component at 0.05 Hz related to the control input and shows the coupling between rolling and yawing of the canopy during turns. The 1.05 Hz payload twist mode does not appear in the parafoil yaw rate.

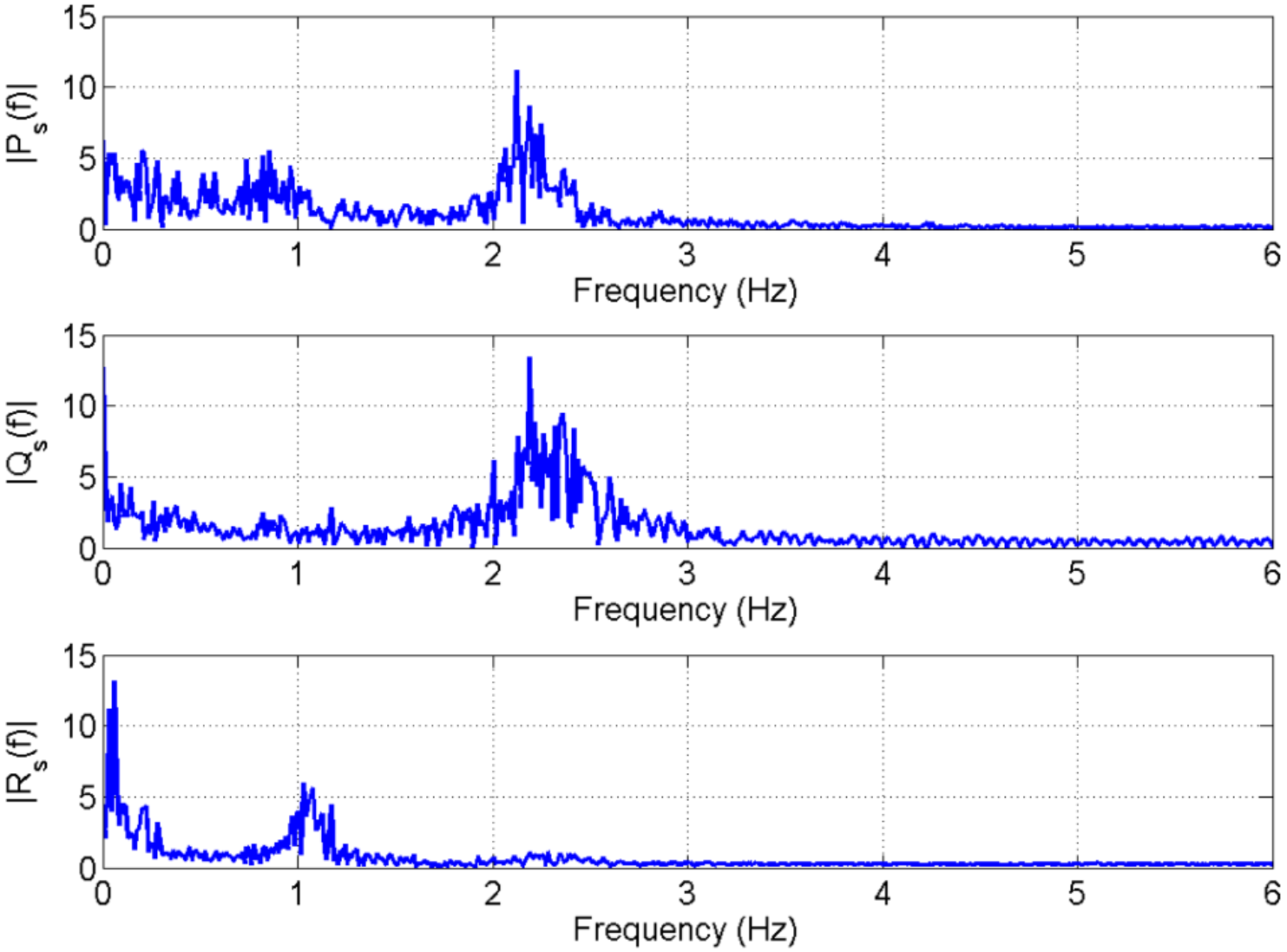

Figure 5.14 Payload angular velocity amplitude spectrum.

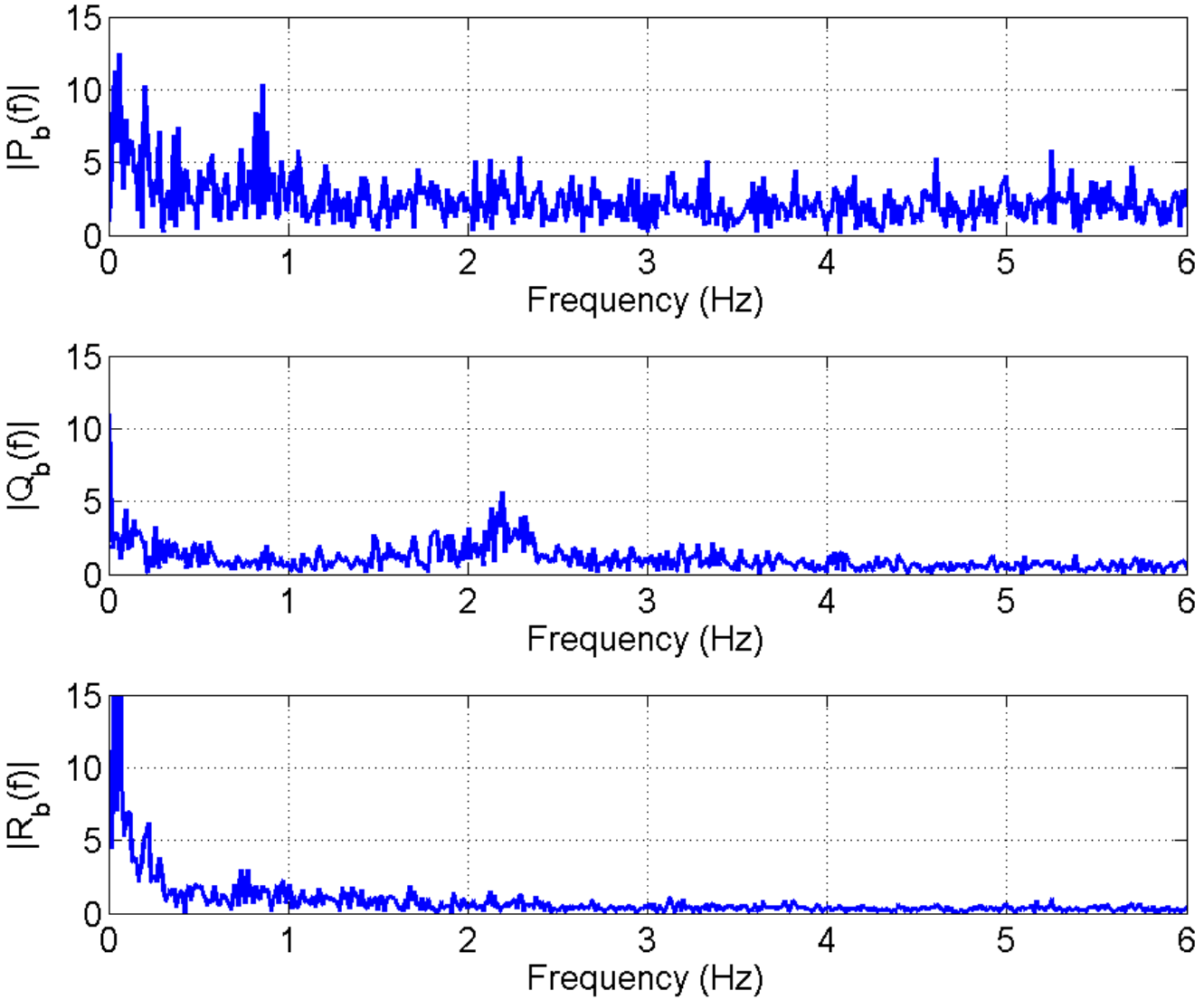

Figure 5.15 Parafoil canopy angular velocity amplitude spectrum.

Canopy sensors located symmetrically on the left and right side of the canopy provide the potential to identify symmetric bending dynamic modes. In contrast to the angular velocity amplitude spectrums in Figures 5.14 and 5.15 where the total canopy angular velocity is the average of left and right sensors, the amplitude spectrum of individual sensors can be investigated. If the canopy rotates as a rigid body then the left and right side sensors would have the same angular velocity with the average having the same amplitude spectrum as each sensor. When the canopy bends, left and right sensors have opposing angular velocities which negate each other as the average is taken. The result being that the bending mode frequency is absent from the average amplitude spectrum but present in the individual sensors. This later case is demonstrate in Figure 5.15 for the canopy bending about its vertical axis where, R_R, R_L, and R_b are the right side canopy rate, left side canopy rate, and average canopy rate amplitude spectrums.

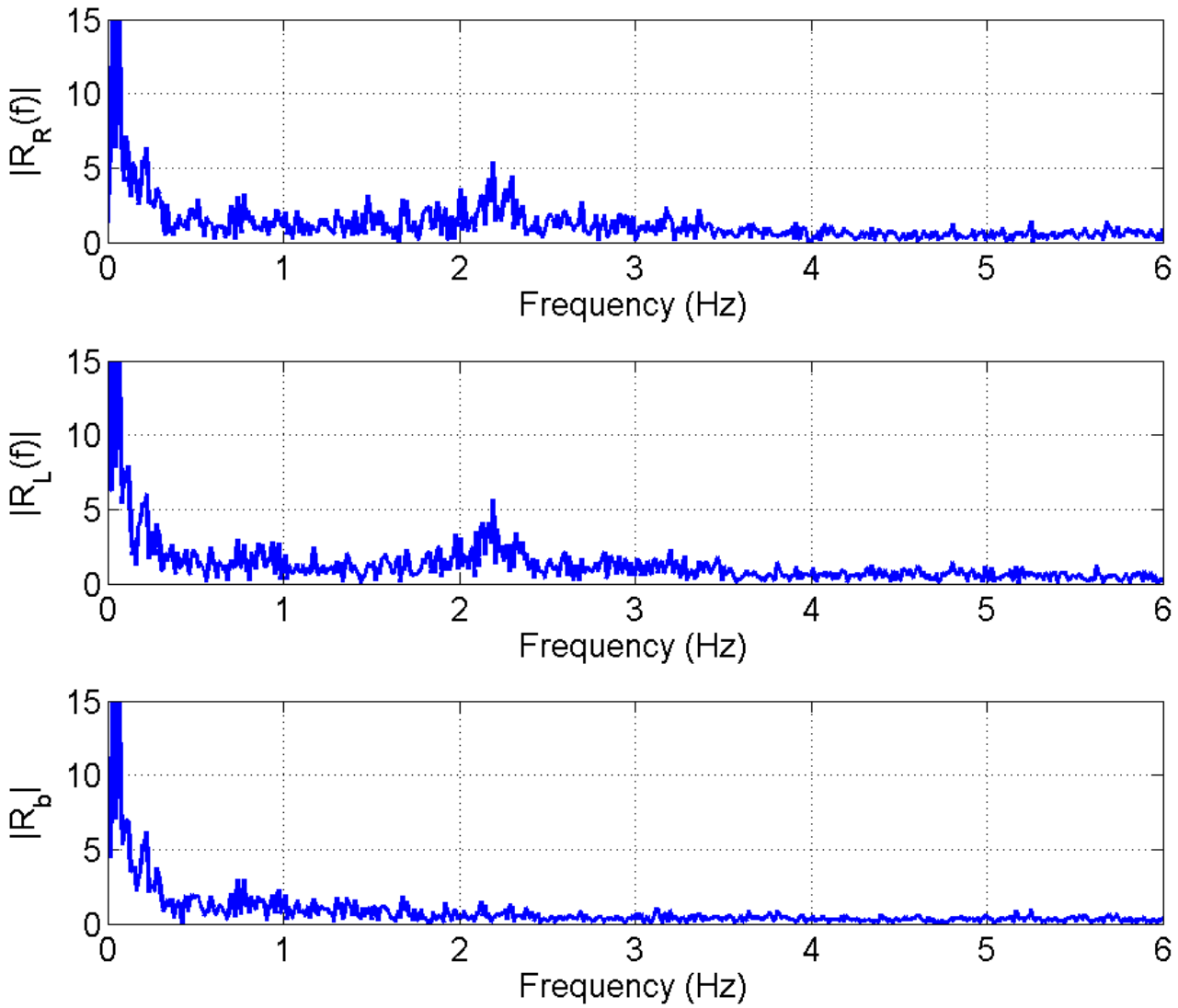

Figure 5.16 Left and right canopy yaw rate amplitude spectrum.

Both left and right sensors exhibit a 0.05 Hz component from the yaw rate commanded by control inputs and smaller 2.2 Hz yaw rate component. When the time domain signals are averaged, the 2.2 Hz components negate each other and only the 0.05 Hz yaw rate mode remains, demonstrating that the canopy has a 0.05 Hz rigid body turning mode and a 2.2 Hz symmetric bending mode. Figure 5.17 illustrates a top view of the canopy motion for this bending phenomenon where the canopy symmetrically bends fore and aft.

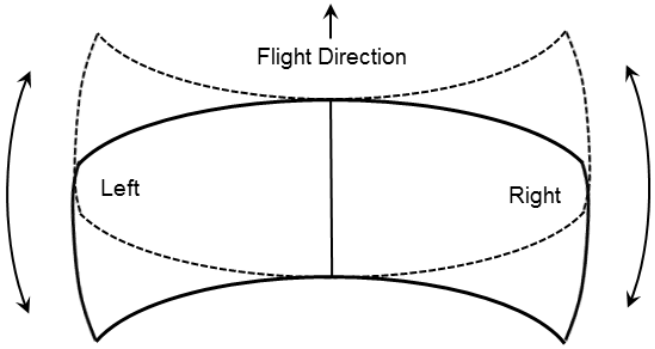

Figure 5.17 Top view of symmetric canopy bending.

The phenomenon is commonly referred to as canopy "breathing." As the canopy breathes in and out, the angle of attack in the tips may change affecting the canopy performance. The inflated fabric airfoil is not a rigid ‘enough’ structure. Fabric is woven in two directions with deformation of that fabric happening mostly diagonal to the weaving directions. The fabric is light weight but the compromise is structure rigidity is lost. Construction of the weave in the fabric leaves weak points around some more rigid points which act like pivot points allowing canopy movement. The canopy breathing frequency is the same as the payload roll and pitch rate frequencies which demonstrate that the payload relative motion may help excite this phenomenon. Analysis of the canopy

roll and pitch rates failed to identify and similar symmetric bending modes suggesting that the canopy is effectively rigid with the exception of a higher frequency symmetric bending or “breathing” mode about its vertical axis, which is small in magnitude compared to the rigid mode.

5.2.3 Parafoil/Payload Motion After Inflation

Comparisons between the payload and parafoil measurements are shown in Figures 5.18 through 5.21. The yaw and yaw rate are separated in two figures because of large twisting motion just after the canopy inflates. During canopy inflation it is common for the payload to twist multiple times before reaching equilibrium. Figure 5.18, starting immediately after canopy inflation, shows the payload yaw rate oscillating with an initial amplitude of 400 deg/s and damping out in 6 to 7 cycles. The parafoil oscillates in response to the payload and line twisting, lagging behind 90 deg in phase, and having significantly smaller initial amplitude of approximately 50 deg/s.

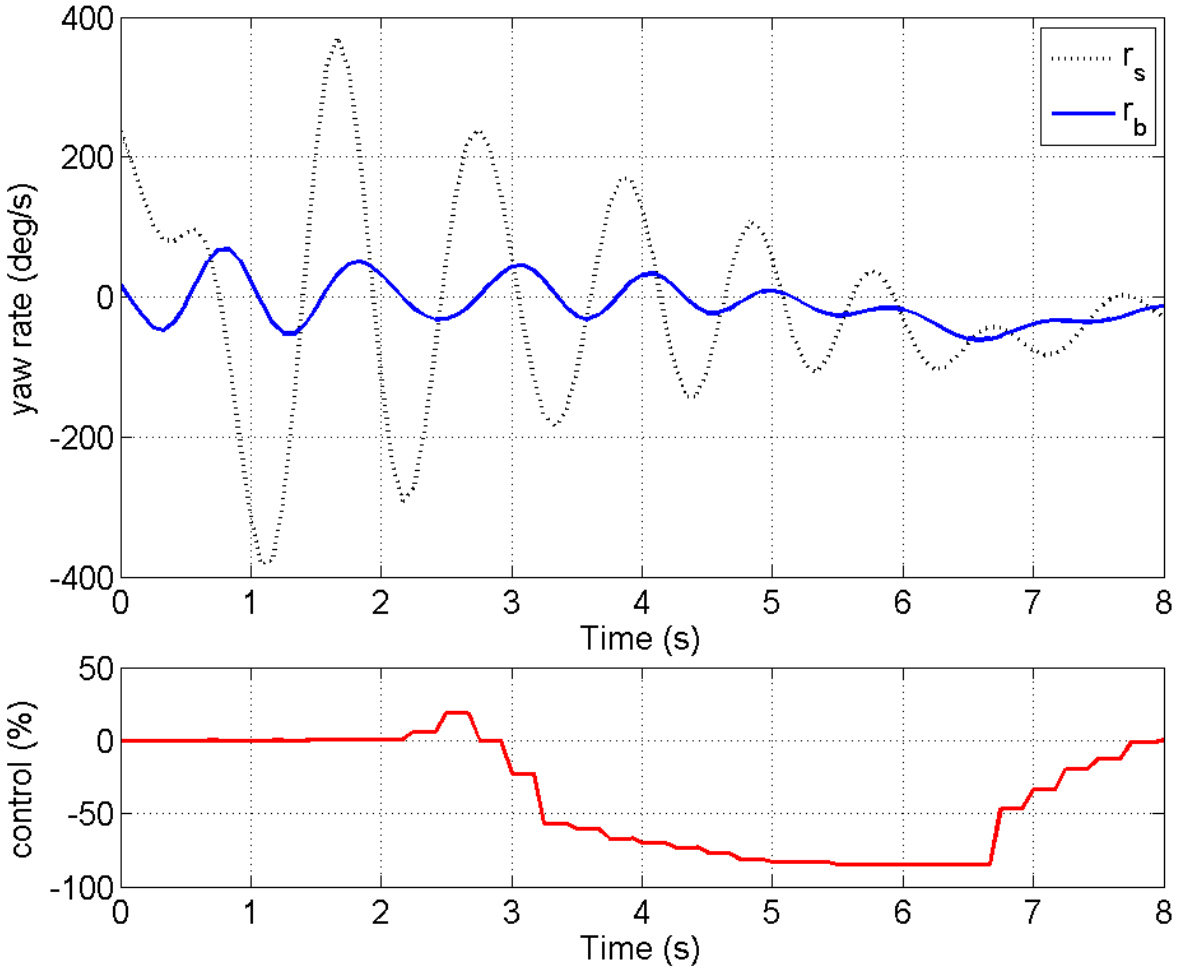

Figure 5.18 Parafoil-payload relative twisting immediately after canopy inflation.

Payload and canopy yaw, yaw rate, and control deflection after the initial payload untwisting are shown below in Figure 5.19. The 1.05 Hz payload twisting mode is clearly evident in the payload yaw rate, r_s, and persists with amplitudes ranging from 20 to 30 deg/s. The payload twisting mode amplitude is on the same order as the main yaw rate during turning. The parafoil also exhibits a small 1.05 Hz oscillation in response to the payload but its amplitude is, 5-10 deg/s, and is very small compared to the larger amplitude yaw rate during turning.

Pitch rates of both the payload and canopy primarily exhibit a 2.2 Hz oscillation that is excited during most of the flight. Throughout most of the turning, the pitch angle remains close to -3 and -10 deg for the payload and parafoil with only small variations as seen in Figure 5.19. Rolling dynamics are shown in Figure 5.20 where differences in the payload and canopy roll rate frequencies can be seen. In contrast to the pitch angle, the payload roll varies by approximately 10 deg as the system turns, with positive roll during a right turn (positive control) and negative roll during a left turn (negative control). The parafoil roll exhibits a similar trend to pitch but experiences more variation.

Common to all measured payload and parafoil angular velocities are the persistent oscillations throughout the flight. In Figure 5.18, the initially large payload yaw rate decays from 400 deg/s to 30 deg/s in 6 to 7 cycles but does not continue to decay to zero. Similarly both pitch and roll rates experience persistent oscillations. This observation is explained by continual disturbance from turbulence and variable winds during flight as evidenced by the many pulses in payload yaw rate in Figure 5.19. As the payload yaw rate begins to decay over 7 cycles it is excited again before reaching equilibrium. Similar dynamics are seen in the pitch and roll rates.

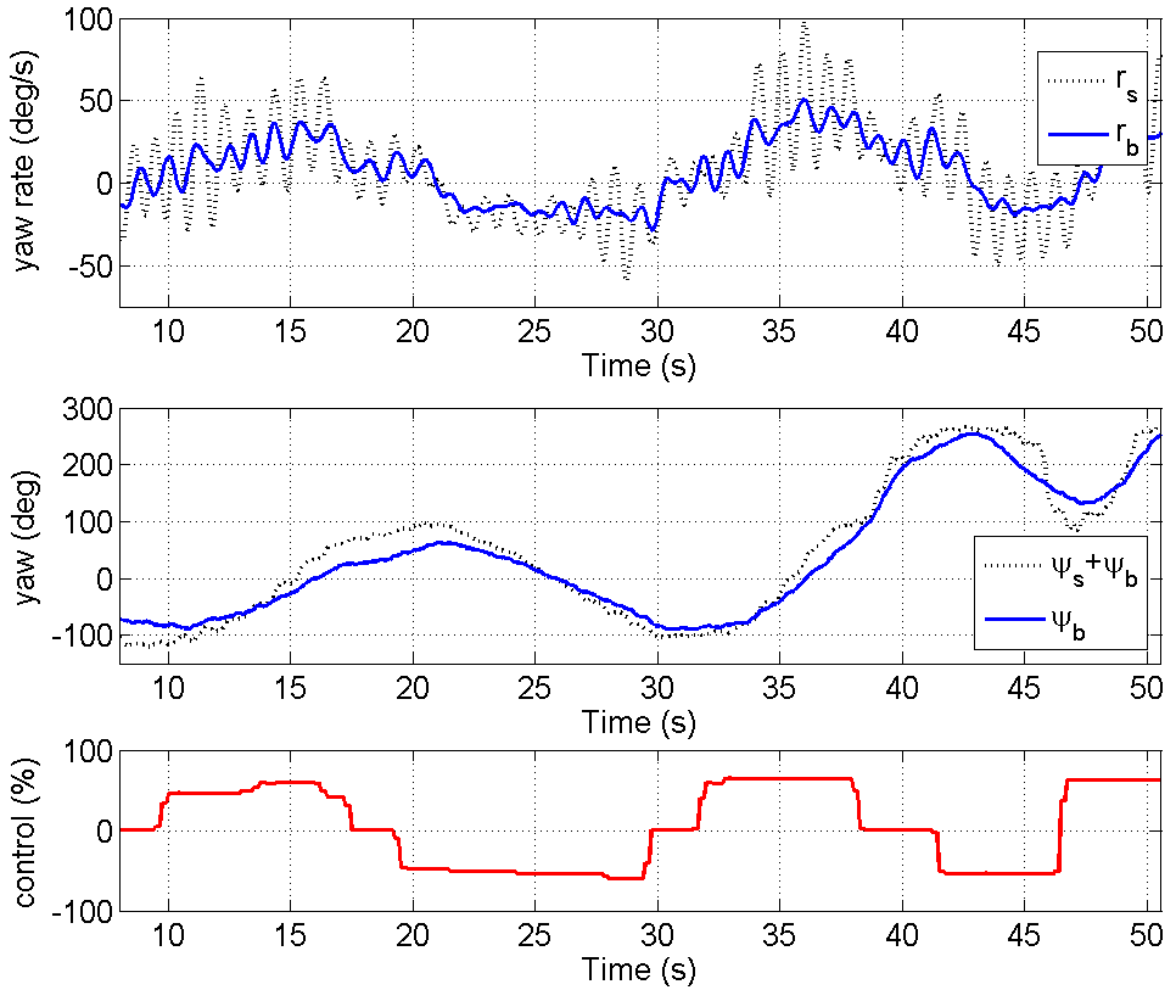

Figure 5.19 Parafoil-payload relative twisting during turning.

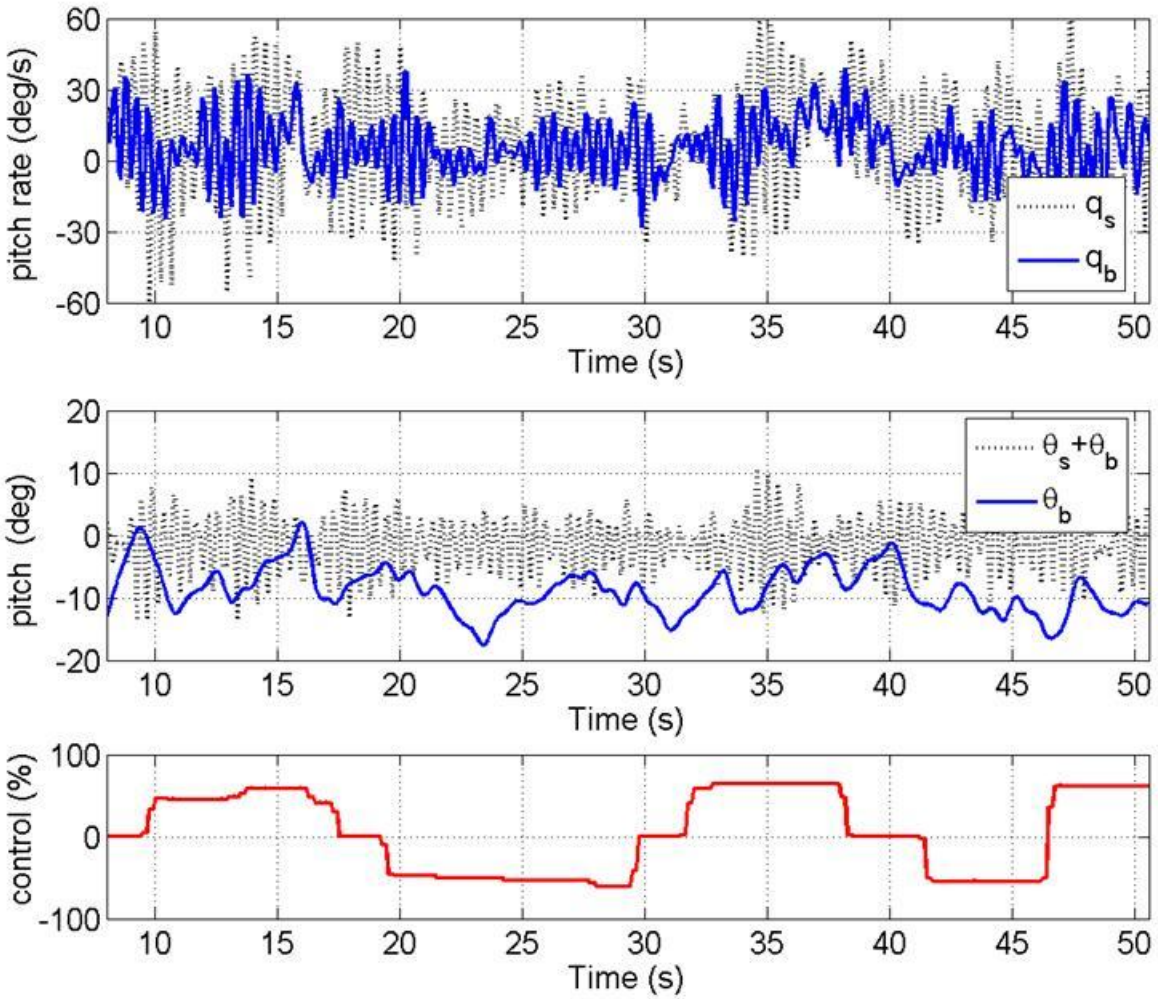

Figure 5.20 Pitch and pitch rate of the parafoil canopy and payload.

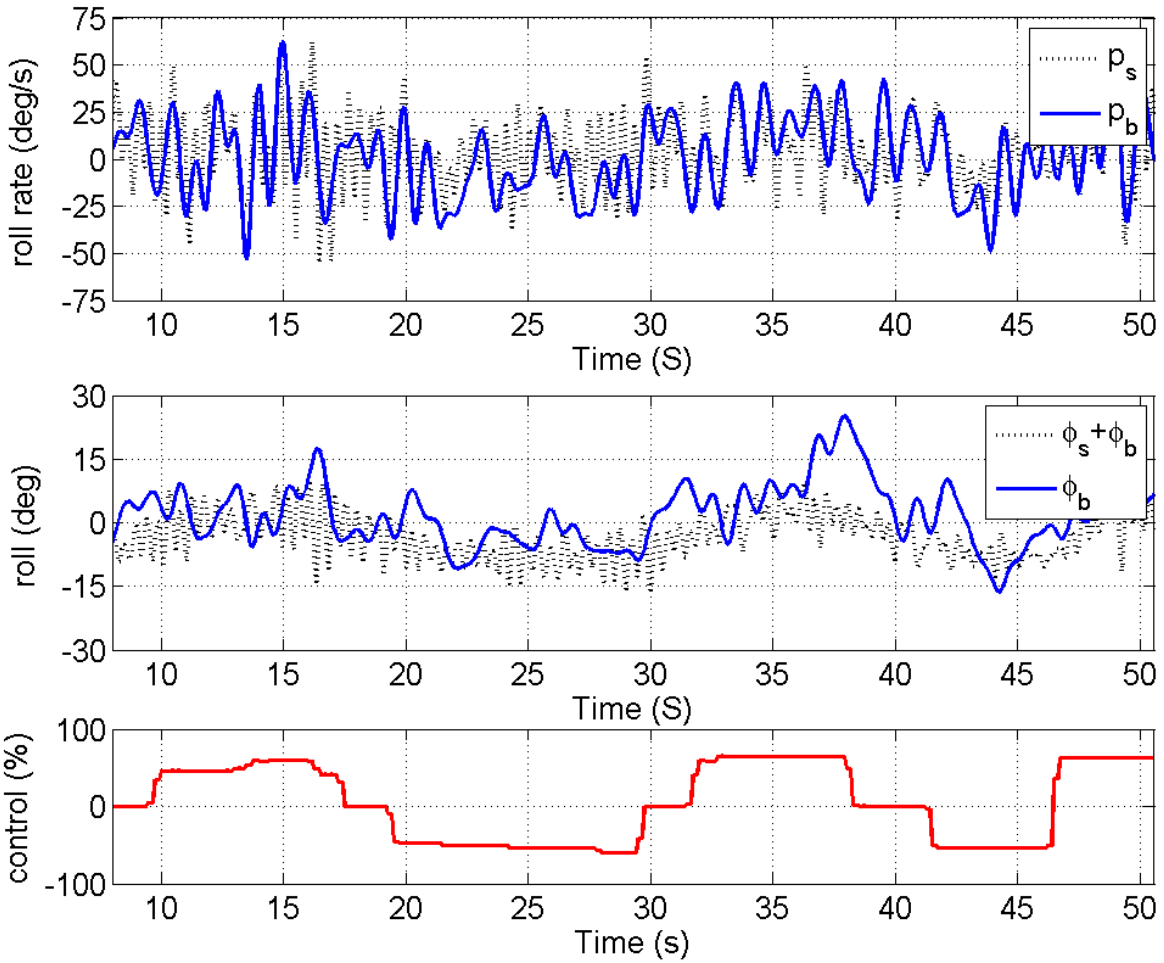

Figure 5.21 Roll and roll rate of the parafoil canopy and payload.

5.3 Experimental and Simulation Comparison Parafoil/Payload Motion

When comparing the simulated results with experimental data, the appearance of persistent oscillation in the experimental data while the simulation decay to a steady state is observed. In the model, only pristine atmospheric conditions were simulated. During experiments, the parafoil experiences changes in wind magnitude, wind direction, updrafts, and turbulence, all exciting motion continually. To simulate a realistic environment experienced in the flight test, a simulated wind profile with turbulence was developed to further validate and compare the model data to the experimental data. The wind profile can be seen in Figure 5.22 and 5.23.

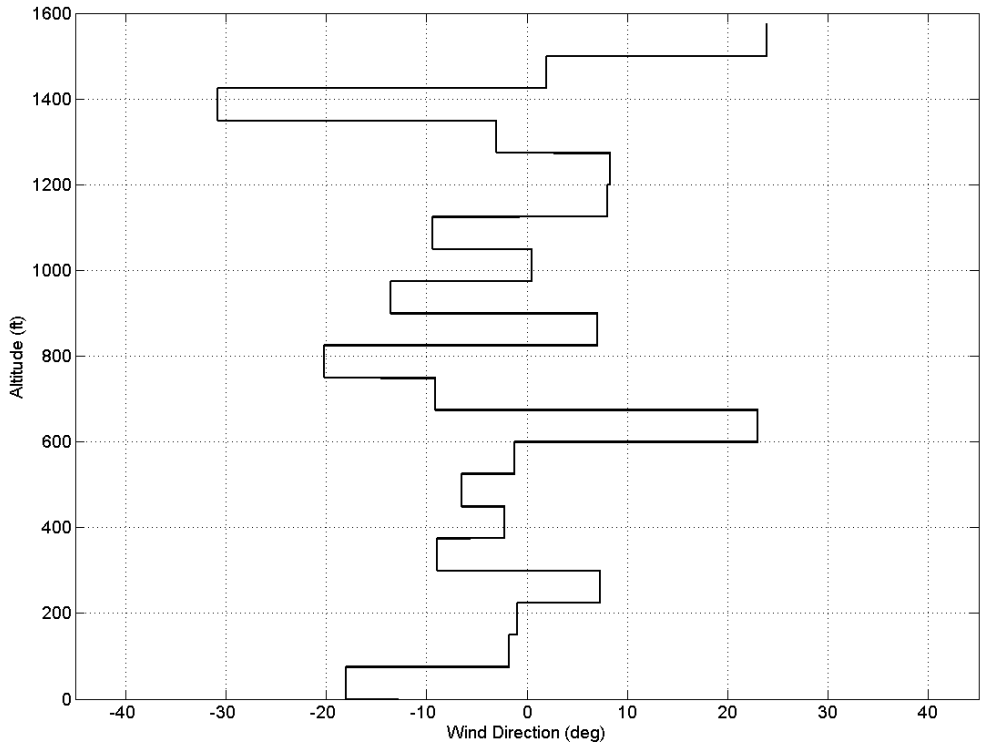

Figure 5.22 Wind direction.

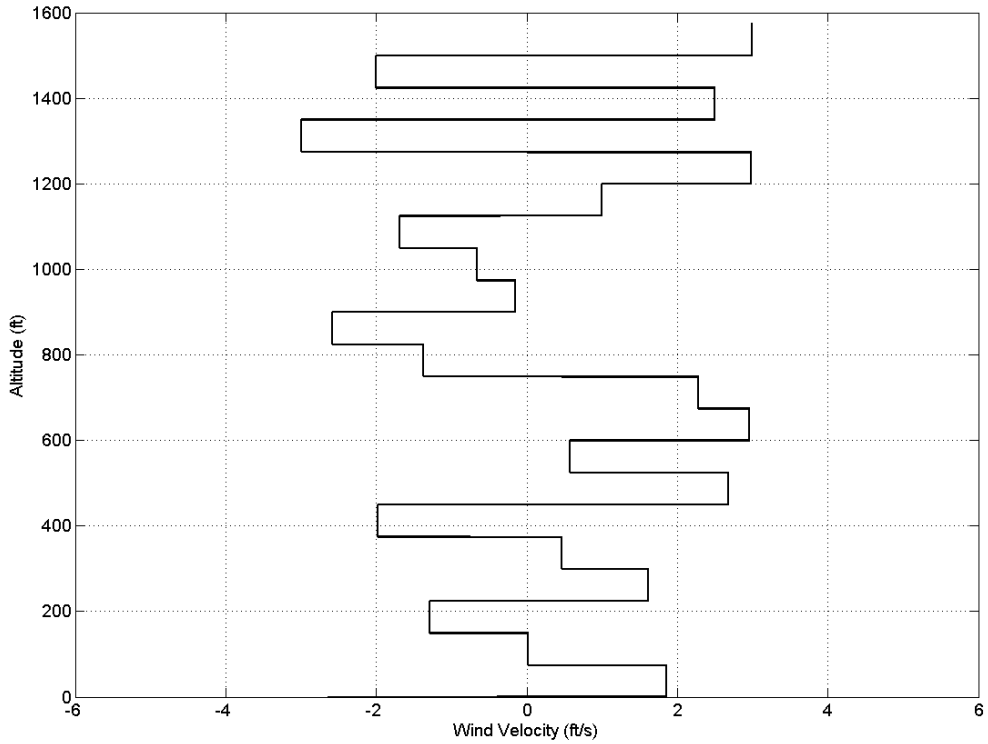

Figure 5.23 Wind velocity magnitude.

The 9-DOF model was chosen to display the results of the addition of atmospheric disturbances and turbulence. When the payload motion is excited in the simulation, the natural oscillations of the parafoil-payload can be seen in Figure 5.24-5.26 below. Similar to the experimental data, the new simulation output demonstrates the 2.2 Hz frequency of the roll rate and pitch rate of the payload and the 1 Hz frequency of the parafoil roll and pitch rate. The coupling between parafoil yaw and roll rate can be seen as the motion is excited by continual changes in the wind. Both the parafoil and payload yaw rate have a frequency of 1 Hz from the twist of the lines.

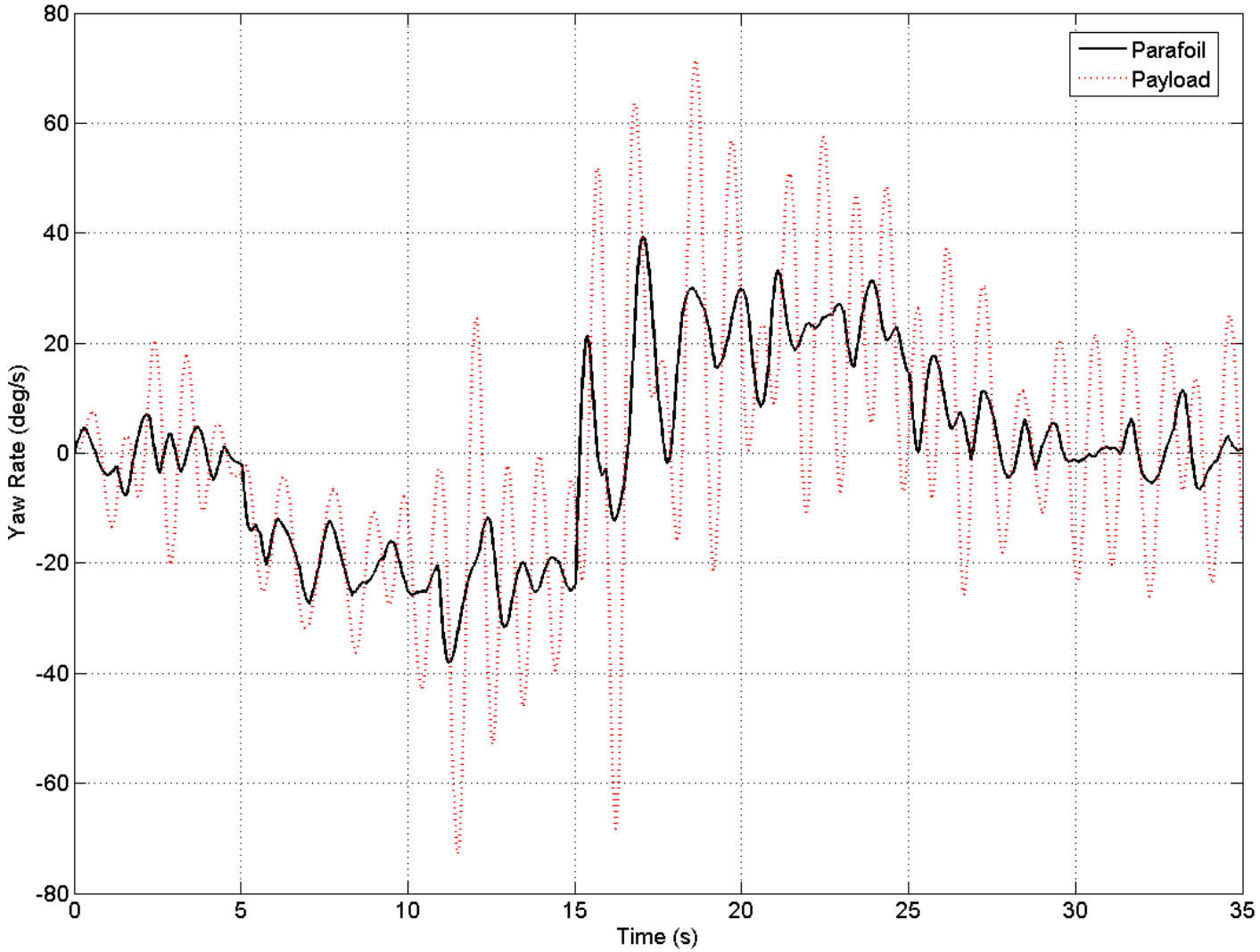

Figure 5.24 9-DOF yaw rate including wind.

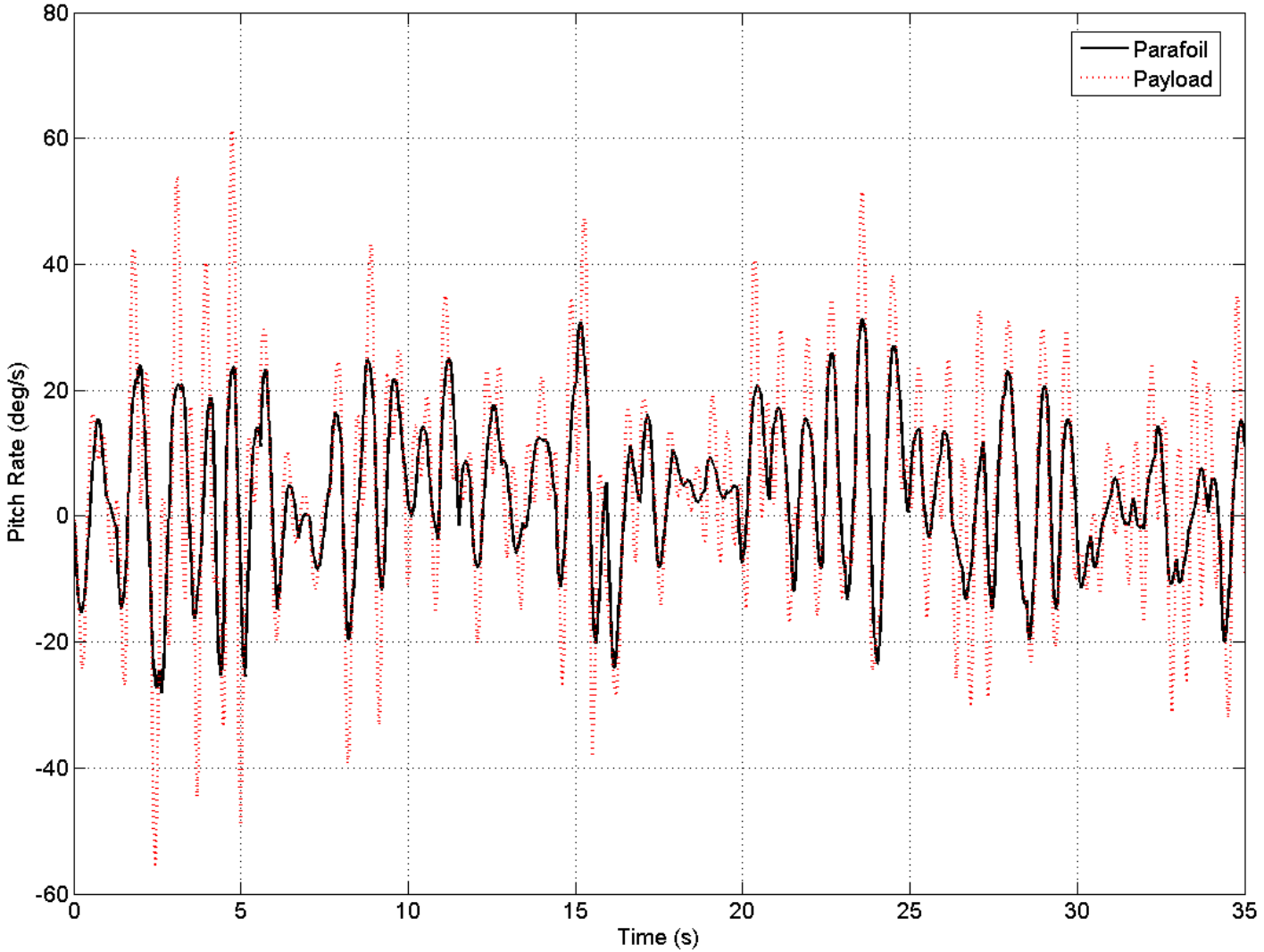

Figure 5.25 9-DOF pitch rate including wind.

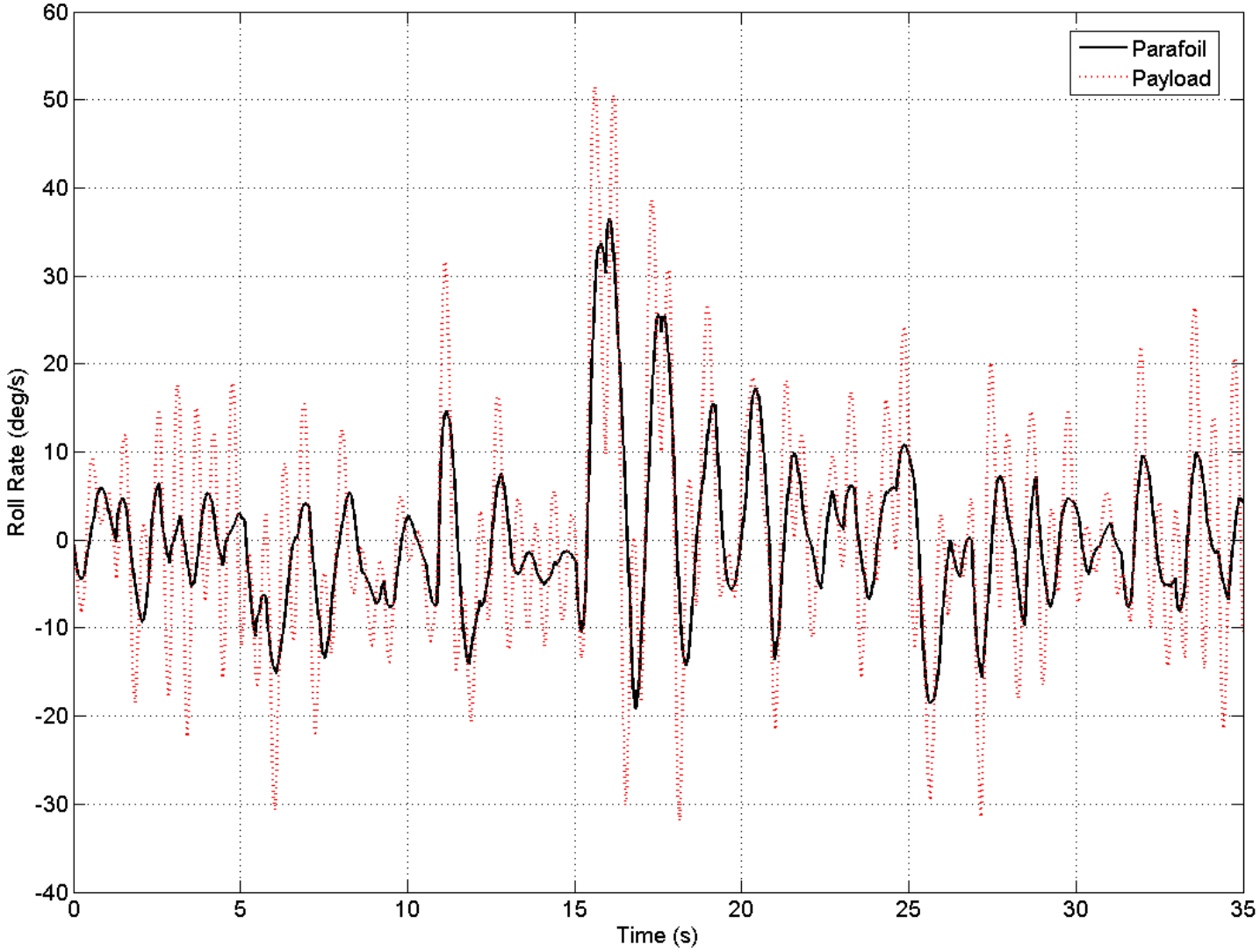

Figure 5.26 9-DOF roll rate including wind

CHAPTER 6

LINEARIZATION

6.1 Linearization

As seen from the previous chapters, only payload relative yawing motion affect the trajectory of the system. This effect is particularly pronounced in the case of large inertial ratio. It can be assumed that for these cases, the 6-DOF and 7-DOF models will be the most concise while still representing all significant motion. Equations of motion for the parafoil models were derived using the same states and procedure as conventional aircraft flight mechanics. In addition, the aerodynamic model takes the same form as conventional aircraft with the addition of apparent mass, which could be modeled using standard aerodynamic coefficients with a conventional aircraft. The following systems are linearized about the initial condition discussed in the previous results.

6.2 Test System

The 6-DOF parafoil model can be separated into a fourth order longitudinal system (u_C, w_C, q_B, θ_B) and a fifth order lateral system (v_C, ϕ_B, p_B, ψ_B, r_B) when linearized. The 6-DOF longitudinal system can be described by the following equation.

$$\begin{Bmatrix} \dot{u_c} \\ \dot{w_c} \\ \dot{q_B} \\ \dot{\theta_B} \end{Bmatrix} = \begin{bmatrix} -0.542 & 0.619 & -10.7 & -30.3 \\ -1.032 & -2.11 & 29.7 & 2.72 \\ 1.293 & -1.622 & -5.42 & -3.72 \\ 0 & 0 & 1 & 0 \end{bmatrix} \begin{Bmatrix} u_c \\ w_c \\ q_B \\ \theta_B \end{Bmatrix} + \begin{bmatrix} 0 \\ 0 \\ 0 \\ 0 \end{bmatrix} \delta_a \tag{6.1}$$

with eigenvalues of -3.33 ± 7.72i and -0.71 ± 1.22i representing both a short period and phugoid mode, respectively. The short period mode has a natural frequency and damping

ratio of 1.34 Hz and 0.39 while the phugoid mode has a natural frequency and damping ratio of 0.23 Hz and 0.50.

Similarly the lateral dynamics become

$$\begin{Bmatrix} \dot{v_c} \\ \dot{\phi_B} \\ \dot{p_B} \\ \dot{\psi_B} \\ \dot{r_B} \end{Bmatrix} = \begin{bmatrix} -0.389 & 30.4 & 12.3 & 0 & -31.6 \\ 0 & 0 & 1 & 0 & -0.141 \\ -0.731 & -2.87 & -6.61 & 0 & -0.248 \\ 0 & 0 & 1 & 0 & 1.01 \\ 0.295 & -0.230 & -2.05 & 0 & -2.43 \end{bmatrix} \begin{Bmatrix} v_c \\ \phi_B \\ p_B \\ \psi_B \\ r_B \end{Bmatrix} + \begin{bmatrix} -0.027 \\ 0 \\ -0.101 \\ 0 \\ 0.524 \end{bmatrix} \delta_a \qquad (6.2)$$

and have four nonzero eigenvalues, two real and one complex conjugate pair, representing the typical roll subsidence, spiral, and dutch roll modes. The roll subsidence and spiral mode eigenvalues are –6.85 and -0.716 with a time constant of 0.15 s and 1.40 s, respectively. Dutch roll eigenvalues are -0.93 ± 4.51i representing a natural frequency and damping ratio of 0.91 Hz and 0.17.

As seen in the first section of Chapter 5, a 6-DOF model would be adequate to capture the motion of a system with if the inertia of the payload is not too much larger than that of the parafoil. If the inertia is larger, the 7-DOF is the minimum degree that captures the change in trajectory. This case will be discussed in the next section, however, for all practical purposes only the linearization of the 7-DOF need be considered.

The 7-DOF parafoil model can also be linearized and separated into a fourth order longitudinal system (u_C, w_C, q_B, θ_B). Linearizing the 7-DOF model about the same initial conditions results in the longitudinal system

$$\begin{Bmatrix} \dot{u_c} \\ \dot{w_c} \\ \dot{q_B} \\ \dot{\theta_B} \end{Bmatrix} = \begin{bmatrix} -0.542 & 0.619 & -10.7 & -30.3 \\ -1.03 & -2.12 & 29.7 & 2.72 \\ 1.29 & -1.62 & -5.41 & -3.72 \\ 0 & 0 & 1 & 0 \end{bmatrix} \begin{Bmatrix} u_c \\ w_c \\ q_B \\ \theta_B \end{Bmatrix} + \begin{bmatrix} 0 \\ 0 \\ 0 \\ 0 \end{bmatrix} \delta_a, \qquad (6.3)$$

where the short period mode eigenvalues -3.34 ± 7.71i and a natural frequency and damping ratio of 1.34 Hz and 0.39 while the phugoid mode eigenvalues are -0.71 ± 1.22i and have natural frequency and damping ratio of 0.23 Hz and 0.50. The 7-DOF lateral dynamics now include two additional states, ψ_S and r_S, and is a seventh order system (v_C, ϕ_B, p_B, ψ_B, r_B, ψ_S, r_S)

$$\begin{Bmatrix} \dot{v}_c \\ \dot{\phi}_B \\ \dot{p}_B \\ \dot{\psi}_B \\ \dot{r}_B \\ \dot{\psi}_S \\ \dot{r}_S \end{Bmatrix} = \begin{bmatrix} -0.391 & 30.4 & 12.3 & 0 & -31.6 & -0.236 & 0 \\ 0 & 0 & 1 & 0 & -0.141 & 0 & 0 \\ -0.735 & -2.86 & -6.58 & 0 & -0.214 & -0.702 & 0 \\ 0 & 0 & 1 & 0 & 1.01 & 0 & 0 \\ 0.329 & -0.256 & -2.28 & 0 & -2.71 & 4.34 & 0 \\ 0 & 0 & 0 & 0 & -1 & 0 & 1 \\ 0 & 0 & 0 & 0 & 0 & -37.3 & 0 \end{bmatrix} \begin{Bmatrix} v_c \\ \phi_B \\ p_B \\ \psi_B \\ r_B \\ \psi_S \\ r_S \end{Bmatrix} + \begin{bmatrix} -0.031 \\ 0 \\ -0.110 \\ 0 \\ 0.584 \\ 0 \\ 0 \end{bmatrix} \delta_a \tag{6.4}$$

having six nonzero eigenvalues, two real and two complex conjugate pairs, representing the roll subsidence, spiral, dutch roll, and an additional payload twist mode. The 7-DOF roll subsidence and spiral mode eigenvalues are -6.92 and -0.72 with a time constant of 0.15 s and 1.40 s. The dutch roll eigenvalues of -0.79 ± 4.41i with a natural frequency and damping ratio of 0.71 Hz and 0.09, In addition, there is an extra second order mode from the payload relative twist which has eigenvalues of -0.230 ± 6.59i representing a natural frequency and damping ration of 1.05 Hz and 0.04. For further comparison, these values have been placed in Table 6.1.

Table 6.1 Comparison of Flight Dynamic Modes

	6-DOF			7-DOF		
	Second Order		First Order	Second Order		First Order
	ω_n (Hz)	ζ	t_c (s)	ω_n (Hz)	ζ	t_c (s)
Longitudinal Modes						
Short Period	1.34	0.40	-	1.34	0.40	-
Phugoid	0.23	0.50	-	0.23	0.50	-
Lateral Modes						
Roll Subsidence Mode	-	-	0.15	-	-	0.14
Spiral Mode	-	-	1.40	-	-	1.40
Dutch Roll	0.73	0.11	-	0.71	0.09	-
Payload Twist	-	-	-	1.05	0.04	-

The 7-DOF longitudinal modes and the first order lateral modes remain virtually unchanged from the 6-DOF system. In contrast, by including payload relative twist, the dutch roll natural frequency and damping ratio of 3% and 18% reduction, respectively. For our test system, neglecting the relative payload-canopy twist results in a slight overestimation of dutch roll mode damping which can be ignored. All other modes remain essentially unchanged which often leads to the assumption that a 6-DOF model can be effectively used for guidance development as in [2] and [11].

6.3 Large Payload Inertia Case

As discussed in Chapter 5, the payload is generally much more massive than the canopy. Using the same method above, a system with a large payload was linearized and a table of comparison can be seen below.

Table 6.2 Comparison of Flight Dynamic Modes for Large Payload System

	6-DOF			7-DOF		
	Second Order		First Order	Second Order		First Order
	ω_n (Hz)	ζ	t_c (s)	ω_n (Hz)	ζ	t_c (s)
Longitudinal Modes						
Short Period	1.34	0.40	-	1.34	0.40	-
Phugoid	0.23	0.50	-	0.23	0.50	-
Lateral Modes						
Roll Subsidence Mode	-	-	0.17	-	-	0.15
Spiral Mode	-	-	1.84	-	-	1.75
Dutch Roll	0.49	0.08	-	0.21	0.02	-
Payload Twist	-	-	-	0.82	0.19	-

In this case, the difference between parafoil and payload motion is more obvious. The 6-DOF model overestimates dutch roll natural frequency by 57% and the damping by 75%. Sensors in the payload will greatly underestimate the movement of the payload when the payload inertia is greater that the parafoil. When guidance feedback is derived from sensors (usually yaw and yaw rate) in the payload, the sensors will be acutely sensitive to the payload oscillatory mode which is very lightly damped and care must then be taken to include the payload oscillatory mode during guidance design.

CHAPTER 7

CONCLUSIONS

While the parafoil/payload system can be modeled with various degrees-of-freedom based on the connection configuration and rigging geometry of the two primary bodies, the complexity of these models may not add value to the control of the system. Many different DOF models have been developed in literature with the absence of the 7-DOF model. The difference in convention and variable definition make comparison of the models in literature difficult. The 7-DOF model was developed to fill in the gap in literature and the 6/8/9-DOF models were generated in parallel to ensure general similarity in development for comparison. The models created were able to simulate parafoil and payload dynamics similar to data gathered by miniature wireless inertial sensors.

The Bantam sensors were developed and used to measure the relative canopy-payload motion. For the first time, direct data from the canopy was obtained and used to verify and analyze multi-body models. For instance, canopy 'breathing' motion can be seen from the gathered data which can change the periphery angle of attack affecting the canopy performance. It is theorized that relative payload motion may excite this phenomenon due similarities in the breathing, roll and pitch rate frequencies.

The experimental data also showed persistence oscillations due to wind changes which have not been seen in models generated. The addition of a wind profile and turbulence to the simulation provided a realistic view of effect of wind on dynamics which can be further developed in the future.

From the experimental data, significant yawing motion between the parafoil and payload could be seen while many of the other dynamic modes exhibit little change for this canopy/payload rigging connection. If the system uses only GPS for its trajectory control, then the 6-DOF model is adequate. However, if control is based on yaw and yaw rate information from payload sensors, the motion of the payload becomes significant as the payload oscillates and may give incorrect readings.

For a common parafoil system with a large payload, the 7-DOF models included all significant dynamics, mainly the payload twist. Other dynamic motion may be important for a different payload connection configuration or if a payload is oddly shaped causing different forces to move the payload. In such a case, the Bantam sensor data would be an immense assistance.

Classical flight dynamic modes were also developed for the rigid (6-DOF) and the relative yaw (7-DOF) parafoil-payload system which was not previously considered by literature. The 6-DOF model has conventional flight modes including, short period and phugoid longitudinal modes and roll subsidence, spiral, and dutch roll lateral modes, like an aircraft. The 7-DOF model is shown to have an additional lightly damped lateral payload mode. This additional mode introduces reduced damping of the payload compared to the rigid model which is important in payload senor controlled guidance. The 7-DOF mode also demonstrates a much lower dutch roll mode than the 6-DOF model. Therefore, the 6-DOF model will overestimate dutrch roll in the system.

REFERENCES

[1] Meyer, J. "An Introduction to Deployable Recovery Systems," *Sandia Report*, 1985.

[2] Pepper, W., Maydew, R., "Aerodynamic Decelerators-An Engineering Review," *Journal of Aircraft*, Vol. 8, No. 1, 1971, pp 3-19.

[3] Jalbert, D. "Multi-Cell Wing Type Aerial Device," *Patent Office 3285546*, Nov.1966.

[4] Nicolaides, J., Speelman, R., Menard, G., "A Review of Parafoil Applications," *Journal of Aircraft*, Vol.7, No. 5, Sept/Oct 1970, pp 423-431.

[5] Machin, R. "Design and Testing of the X-38 Spacecraft Primary Parafoil," *AIAA Paper 2000-4312*, Aug. 2000.

[6] Benney, R., Henry, M., Lafond, K., Meloni, A., "DOD New JPADS Programs & NATO Activities," *AIAA Paper 2009-2952*, May 2009.

[7] Adam, P., Duchemin, O., Mason, R., Noca, M., "Autonomous Parafoils for the Exploration of Outer Planet Atmospheres," *AIAA Paper 1997-1428*, June 1997.

[8] Jann, T., "Advanced Features for Autonomous Parafoil Guidance, Navigation and Control," *AIAA Paper 2005-1642*, May 2005.

[9] Slegers, N., Costello, M., "Model Predictive Control of a Parafoil and Payload System," *Journal of Guidance, Control, and Dynamics*, Vol. 28, No. 4, 2005, pp. 816-821.

[10] Barrows, T., "Apparent Mass of Parafoils with Spanwise Camber," *Journal of Aircraft*, Vol. 39, No. 3, 2002, pp. 445-451.

[11] Slegers, N., Beyer, E., and Costello, M., "Use of Variable Incidence Angle for Glide Slope Control of Autonomous Parafoil," *Journal of Guidance, Control, and Dynamics*, Vol. 31, No. 3, 2008, pp. 585-596.

[12] Müller, S. Wagner, O., Sachs, G., "A High-Fidelity Nonlinear Multibody Simulation Model for Parafoil Systems," *AIAA Paper 2003-2120*, May 2003.

[13] Redelinghuys, R., "A Flight Simulation Algorithm for a Parafoil Suspending an Air Vehicle," *Journal of Guidance, Control, and Dynamics*, Vol. 30, No. 3, 2007, pp. 791-803.

[14] Slegers, N., "Effects of Canopy-Payload Relative Motion on Control of Autonomous Parafoil," *Journal of Guidance, Control, and Dynamics*, Vol. 33, No. 1, 2010, pp. 116-125.

[15] Mooij, E. Wijnands, Q.G.J., Schat, B., "9 dof Parafoil/Payload Simulator Development and Validation," *AIAA Paper 2003-5459*, Aug 2003.

[16] Strickert, G., and Jann, T., "Determination of the Relative Motion Between Parafoil Canopy and Load Using Advanced Video-Image Processing Techniques," *AIAA Paper 99-1754*, May 1999.

[17] Lissaman, P., and Brown, G., "Apparent Mass Effects on Parafoil Dynamics," *AIAA Paper 93-1236*, May 1993.

[18] Lamb, H., "Hydrodynamics," Dover, New York, 1945, pp. 160–174.

[19] Slegers, N., and Yakimenko, O., "Terminal Guidance of Autonomous Parafoils in High Wind to Airspeed Ratios," *Journal Aerospace Engineering IMechE*, Part G, Vol. 225, No. 3, pp. 336-346, 2011.

[20] Atair Aerospace, Picture of Onyx Ultra Light, "The Future of Parachute Technology", http://www.atair.com.

[21] Federation of American Scientists, Picture of GPADS, "Guided Parafoil Air Deliver System – Light", http://www.fas.org/man/dod-101/sys/ac/equip/gpads-l.htm

[22] United States Parachute Association, Picture of pyramid-shaped parachute, "Skydiving History", http://www.uspa.org/AboutSkydiving/SkydivingHistory/

[23] Military Daily News, Picture of JPADS, "JPADS: Making Precision Air-Drops A Reality", http://militarydailynews.com/2010/06/jpads-making-precision-air-drops-a-reality

[24] Airborne Systems, Picture of MegaFly, "Delivering Supplies for Distributed Operations with Parachute Aerial Delivery Systems", http://www.armedforces-int.com/article/delivering-supplies-for-distributed-operations.html